



Publication Year	2019
Acceptance in OA @INAF	2021-04-16T15:30:48Z
Title	Massive star cluster formation under the microscope at $z = 6$
Authors	VANZELLA, Eros; CALURA, Francesco; MENEGHETTI, MASSIMO; CASTELLANO, MARCO; Caminha, G. B.; et al.
DOI	10.1093/mnras/sty3311
Handle	http://hdl.handle.net/20.500.12386/30776
Journal	MONTHLY NOTICES OF THE ROYAL ASTRONOMICAL SOCIETY
Number	483

Massive star cluster formation under the microscope at $z = 6$

E. Vanzella,^{1★} F. Calura,^{1★} M. Meneghetti,¹ M. Castellano,² G. B. Caminha,³
A. Mercurio,⁴ G. Cupani,⁵ P. Rosati,^{1,6} C. Grillo,⁷ R. Gilli,¹ M. Mignoli,¹
G. Fiorentino,¹ C. Arcidiacono,¹ M. Lombini¹ and F. Cortecchia¹

¹INAF – OAS, Osservatorio di Astrofisica e Scienza dello Spazio di Bologna, via Gobetti 93/3, I-40129 Bologna, Italy

²INAF – Osservatorio Astronomico di Roma, via Frascati 33, I-00078 Monte Porzio Catone (RM), Italy

³Kapteyn Astronomical Institute, University of Groningen, Postbus 800, NL-9700 AV Groningen, the Netherlands

⁴INAF – Osservatorio Astronomico di Capodimonte, via Moiaranello 16, I-80131 Napoli, Italy

⁵INAF – Osservatorio Astronomico di Trieste, via G. B. Tiepolo 11, I-34143 Trieste, Italy

⁶Dipartimento di Fisica e Scienze della Terra, Università degli Studi di Ferrara, via Saragat 1, I-44122 Ferrara, Italy

⁷Dipartimento di Fisica, Università degli Studi di Milano, via Celoria 16, I-20133 Milano, Italy

Accepted 2018 November 30. Received 2018 November 30; in original form 2018 September 3

ABSTRACT

We report on a superdense star-forming region with an effective radius (R_e) smaller than 13 pc identified at $z = 6.143$ and showing a star formation rate density $\Sigma_{\text{SFR}} \sim 1000 \text{ M}_{\odot} \text{ yr}^{-1} \text{ kpc}^{-2}$ (or conservatively $>300 \text{ M}_{\odot} \text{ yr}^{-1} \text{ kpc}^{-2}$). Such a dense region is detected with $S/N \gtrsim 40$ hosted by a dwarf extending over 440 pc, dubbed D1. D1 is magnified by a factor $17.4(\pm 5.0)$ behind the Hubble Frontier Field galaxy cluster MACS J0416 and elongated tangentially by a factor 13.2 ± 4.0 (including the systematic errors). The lens model accurately reproduces the positions of the confirmed multiple images with a rms of 0.35 arcsec. D1 is part of an interacting star-forming complex extending over 800 pc. The SED-fitting, the very blue ultraviolet slope ($\beta \simeq -2.5$, $F_{\lambda} \sim \lambda^{\beta}$), and the prominent Ly α emission of the stellar complex imply that very young ($<10\text{--}100$ Myr), moderately dust-attenuated ($E(B - V) < 0.15$) stellar populations are present and organized in dense subcomponents. We argue that D1 (with a stellar mass of $2 \times 10^7 \text{ M}_{\odot}$) might contain a young massive star cluster of $M \lesssim 10^6 \text{ M}_{\odot}$ and $M_{\text{UV}} \simeq -15.6$ (or $m_{\text{UV}} = 31.1$), confined within a region of 13 pc, and not dissimilar from some local super star clusters (SSCs). The ultraviolet appearance of D1 is also consistent with a simulated local dwarf hosting an SSC placed at $z = 6$ and lensed back to the observer. This compact system fits into some popular globular cluster formation scenarios. We show that future high spatial resolution imaging (e.g. E-ELT/MAORY-MICADO and VLT/MAVIS) will allow us to spatially resolve light profiles of 2–8 pc.

Key words: gravitational lensing: strong – galaxies: formation – galaxies: starburst.

1 INTRODUCTION

The observational investigation of star formation at high redshift ($z \gtrsim 6$) at very small physical scales (at the level of star-forming complexes of $\lesssim 200$ pc including super star clusters, SSCs) is a new challenge in observational cosmology (e.g. Livermore et al. 2015; Dessauges-Zavadsky et al. 2017; Johnson et al. 2017; Rigby et al. 2017; Vanzella et al. 2017b,c; Cava et al. 2018; Dessauges-Zavadsky & Adamo 2018). Thanks to strong gravitational lensing, the possibility to catch and study globular clusters precursors (GCPs) is becoming a real fact, both with statistical studies (e.g.

Elmegreen, Malhotra & Rhoads 2012; Renzini 2017; Vanzella et al. 2017b; Boylan-Kolchin 2018) and by inferring the physical properties of individual objects (e.g. Vanzella et al. 2017b,c). The luminosity function of forming GCs has also been addressed for the first time (Bouwens et al. 2018; Boylan-Kolchin 2018) and their possible contribution to the ionizing background is now under debate (e.g. Ricotti 2002; Schaerer & Charbonnel 2011; Katz & Ricotti 2013; Boylan-Kolchin 2018). While still at the beginning, the open issues of GC formation (e.g. Renzini et al. 2015; Bastian & Lardo 2018; Renaud 2018) and what sources caused reionization (e.g. Yue et al. 2014; Robertson et al. 2015) can be addressed with the same observational approach, at least from the high- z prospective. This is a natural consequence of the fact that the search for extremely faint sources possibly dominating the ionizing background

* E-mail: eros.vanzella@inaf.it (EV); francesco.calura@inaf.it (FC)

(e.g. Yue et al. 2014; Finkelstein et al. 2015; Robertson et al. 2015; Alavi et al. 2016; Bouwens et al. 2016a,b; Dayal & Ferrara 2018) plausibly matches the properties a GCP would have both in terms of stellar mass and luminosity (e.g. Schaerer & Charbonnel 2011; Renzini 2017; Bouwens et al. 2018; Boylan-Kolchin 2018) and this eventually depends on the different GCP formation scenarios (Renzini et al. 2015; Ricotti, Parry & Gnedin 2016; Li et al. 2017; Renzini 2017; Bastian & Lardo 2018; Kim et al. 2018; Zick, Weisz & Boylan-Kolchin 2018). A way to access low-luminosity regimes – otherwise not attainable in the blank fields – is by exploiting gravitational lenses. Other than ‘simply’ counting objects at unprecedented flux limits, the strong lensing amplification allow us to probe the structural parameters down to the scale of a few tens of parsec (e.g. Kawamata et al. 2015; Livermore et al. 2015; Rigby et al. 2017; Vanzella et al. 2017b,c) and witness clustered star-forming regions and/or star clusters otherwise not spatially resolved in non-lensed field studies. The lens models are subjected to a strict validation thanks to dedicated simulations and observational campaigns with Hubble (e.g. Meneghetti et al. 2017; Atek et al. 2018) in conjunction to unprecedented (blind) spectroscopic confirmation of hundreds of multiple images with VLT/MUSE¹ in the redshift range $3 < z < 6.7$ (e.g. Caminha et al. 2017a,b; Karman et al. 2017; Mahler et al. 2018). Such analyses are providing valuable insights on the systematic errors on magnification maps. In some (not rare) conditions the uncertainty on large magnification $\mu > 10$ can be significantly lowered to a few per cent by exploiting the measured relative fluxes among multiple images that provide an observational constraint on the relative magnifications (e.g. Vanzella et al. 2017b,c). These methods allow us to determine the absolute physical quantities, like the luminosity, sizes, stellar mass, and star formation rates with uncertainties not dominated by the aforementioned systematics.

A more complex issue is related to the role of such a nucleated star formation on the ionization of the surrounding medium, eventually leaking into the intergalactic medium. Probing the presence of optically thin (to Lyman continuum) channels or cavities which cause the ionizing leakage from these tiny sources (e.g. Behrens, Dijkstra & Niemeyer 2014; Calura et al. 2015) will represent the next challenge. The presence of diffuse Ly α emission (observed as nebulae or haloes or simply offset emissions) often detected around faint sources may provide a first route to address this issue (e.g. Caminha et al. 2016; Leclercq et al. 2017; Vanzella et al. 2017a, see also Gallego et al. 2018), along with the recent detection of ultraviolet high-ionization nebular lines like C IV λ 1548, 1550, He II λ 1640, O III] λ 1661, 1666 or C III] λ 1907, 1909 suggesting that hot stars and/or nuclear contribution might be present, making some sources highly efficient Lyman continuum emitters (e.g. Stark et al. 2014, 2015a,b, 2017; Vanzella et al. 2017c). However, the final answer, especially at $z > 3-6$, will be addressed only with *JWST* by monitoring the spatial distribution of the Balmer lines, and possibly look for induced fluorescence by the Lyman continuum leakage up to the circumgalactic medium and/or to larger distances, i.e. the intergalactic medium (IGM) (e.g. Mas-Ribas et al. 2017).

While giant ultraviolet clumps have been studied at high redshift (e.g. Förster Schreiber et al. 2011; Genzel et al. 2011; Guo et al. 2012; Elmegreen et al. 2013; Cava et al. 2018), the direct observation of young star clusters at cosmological distances is challenging. Given the typical *HST* pixel scale ($0.03 \text{ arcsec pixel}^{-1}$) and spa-

tial sampling (e.g. 0.18 arcsec FWHM of the intergalactic medium (PSF) in the WFC3/F105W band), the most stringent upper limit on the physical size attainable after a proper PSF deconvolution² is $168(84) \text{ pc}$, corresponding to $1.0(0.5)$ pixels at redshift 6, in a non-lensed field. If compared to the typical effective radii of local young massive clusters (YMCs) of $R_e < 20 \text{ pc}$,³ assuming this value holds also at $z = 6$, it becomes clear why strong lensing is crucial if one wants to approach such a scale with *HST*. As shown in Vanzella et al. (2017b,c) the lensing magnification can significantly stretch the image along some preferred direction (up to a factor 20, tangentially or radially with respect to the lens) allowing us to probe the aforementioned small sizes of $10-30 \text{ pc}$. This effect was exploited in a study of a sample of objects behind the Hubble Frontier Field galaxy cluster MACS J0416 (Vanzella et al. 2017b, see also Bouwens et al. 2018). The identification of a very nucleated (or not spatially resolved) object despite a large gravitational lensing stretch is an ideal case where to search for single stellar clusters (and potential GCP). Here, we report on such a case and perform new analysis on a pair of objects already presented in Vanzella et al. (2017b) but with significantly improved size measurements, refined lensing modelling and SED-fitting. The objects discussed in this work, dubbed D1 and T1 at $z = 6.143$, correspond to D1 and GC1 previously reported by Vanzella et al. (2017b). The combination of the main physical quantities like the star formation rate and the sizes reveals an extremely large star formation rate surface densities, lying in a poorly explored region of the Kennicutt–Schmidt (KS) law (Kennicutt 1998b; Bigiel et al. 2010).

In Sections 2.1 and 2.2 the refined lens model, ultraviolet morphology and the physical properties of the system are presented. Using the Ly α properties and the SED-fitting results the emerging dense star formation activity is discussed in Section 2.3. In Section 3, we simulate a local star-forming dwarf hosting a super-star cluster (NGC 1705) to $z = 6.1$ and applying strong lensing. In Section 4, we discuss the results and the identification of a super-star cluster at $z = 6.1$, compared to local YMCs. Section 5 summarizes the main results. We assume a flat cosmology with $\Omega_M = 0.3$, $\Omega_\Lambda = 0.7$ and $H_0 = 70 \text{ km s}^{-1} \text{ Mpc}^{-1}$, corresponding to $5660 \text{ physical parsec}$ for 1 arcsec separation at redshift $z = 6.143$. If not specified, the distances reported in the text are physical.

2 REANALYSING THE $z = 6.143$ SYSTEM IN MACS J0416

2.1 A robust lensing model

In Vanzella et al. (2017b), we used the lens model developed by Caminha et al. (2017a) (see also, Grillo et al. 2015) to infer the intrinsic physical and morphological properties of the system shown in Fig. 1, made by a star-forming complex including the objects D1 and T1 (meaning Dwarf 1 and Tiny 1, respectively). We will refer in the following to the system ‘D1T1’ to indicate the entire system including the stellar stream connecting the two [see Fig. 2, in which much fainter sources, dubbed ‘Ultra Tiny’ (UT), UT1, 2, 3 are also indicated and mentioned in the discussion]. The model

²As can be performed with GALFIT, see simulations reported in Vanzella et al. (2016a, 2017b) and discussion in Peng et al. (2010).

³ $R_e \simeq 1-8 \text{ pc}$ for masses of the clusters of $< 10^6 M_\odot$, e.g. Ryon et al. (2017), or slightly larger radii, $< 20 \text{ pc}$, for those more massive, $> 10^6 M_\odot$ and identified in merging galaxies (Portegies Zwart, McMillan & Gieles 2010; Linden et al. 2017).

¹www.eso.org/sci/facilities/develop/instruments/muse.html (Bacon et al. 2010, 2015).

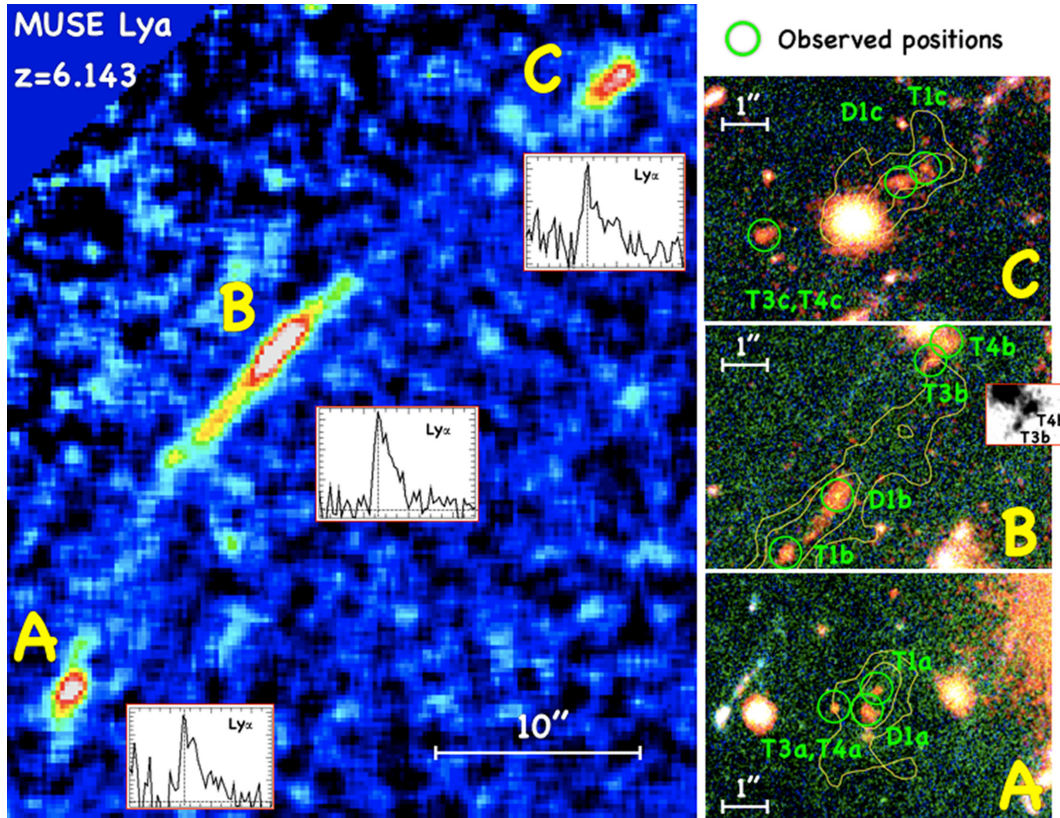


Figure 1. *Left:* The wide Ly α arc (50 arcsec) at $z = 6.143$ observed with MUSE and weighted-averaged over 12 slices ($\Delta v \simeq 500 \text{ km s}^{-1}$). Three multiple images are indicated (A, B, and C, see Caminha et al. 2017a) with their associated Ly α lines extracted from the MUSE spectra. The image B is the most magnified among the three and studied in detail in this work. On the right-hand side, the three panels from top to bottom show the zoomed regions in the colour *HST* image (red channel = F105W, green channel = F814W, and blue channel = F606W) of the main images A, B, and C, including the observed positions (indicated with green circles) of the multiple images of relevant objects (D1, T1, and the T3–T4 pair). The inset in the middle-right panel is the F105W showing the double knot morphology of T3–T4, which is barely detected in the less magnified counter images A and C. The yellow contours show the MUSE Ly α emission at 3σ and 7σ level.

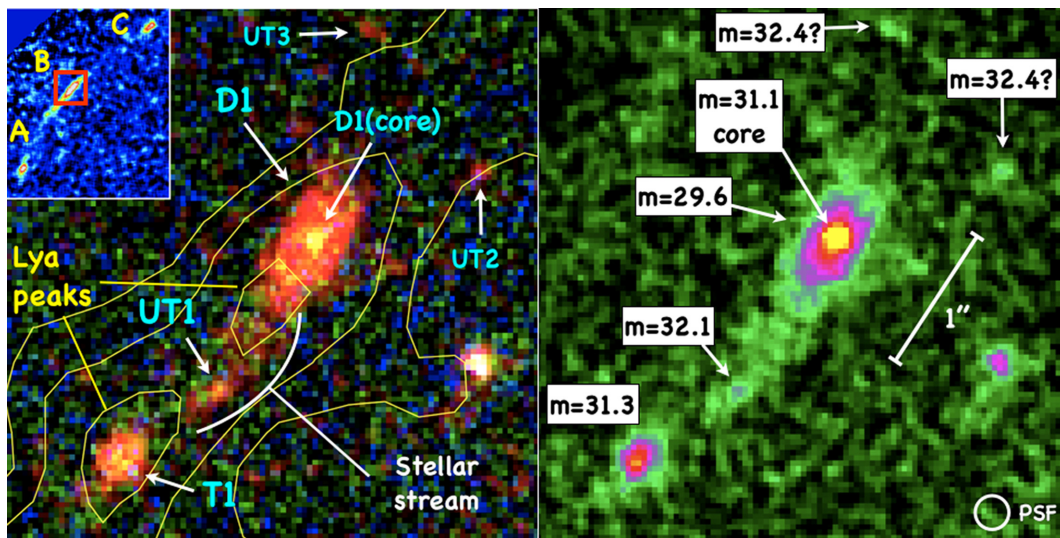


Figure 2. Colour composite (left) and the WFC3/F105W image (right) of the field under study containing the sources D1 and T1. This region corresponds to the red square in the top-left inset which shows the extended Ly α arc from MUSE (see Fig. 1). Sources are labelled (left), along with their de-lensed F105W magnitudes (right). Note the prominent symmetric core of D1 despite the large tangential magnification and the presence of a stellar stream possibly connecting D1 and T1, also including a star-forming knot, dubbed UT1. Other faint knots are shown, UT2 and UT3, with de-lensed magnitudes fainter than 32. The *HST* F105W PSF is shown in the bottom right.

was tuned to reproduce the positions of more than 100 confirmed multiple images, belonging to 37 individual systems, spanning the redshift range 3–6.2. Here, we focus on the system at redshift 6.143 that recently has been further enriched by (at least) 13 individual objects producing more than 30 multiple images all at $z \simeq 6$, some of them already spectroscopically confirmed at the same redshift of D1T1 (such an overdensity will be presented elsewhere) and others still based on robust photometric redshifts (e.g. Castellano et al. 2016). The new systems and the multiple images are also consistent with the expected positions predicted from the aforementioned lens model. An example is the system dubbed T3 and T4, a pair of sources showing the same colours and dropout signature as D1T1 (this object is also present in the Castellano et al. 2016 catalogue with $z_{\text{phot}} \simeq 6$). Indeed, the lens model allows us to reliably identify the multiple images, corroborating also the photometric redshift with the lens model itself. Fig. 1 shows the well spatially resolved T3,T4 pair in the most magnified (tangentially stretched) image B, while the counter-images A and C appear as a single merged object (though image C still shows an elongation, as expected). These new identifications allow us to further tune and better constrain the lens model lowering the uncertainties of the magnification maps at $z = 6$ (an ongoing deep MUSE AO-assisted program, 22h PI: Vanzella, will explore the redshifts of the overdensity). Fig. 1 shows the nine identified multiple images of the system D1T1 and T3–T4 (marked with green circles). The positions are reproduced with an rms of 0.35 arcsec. The same accuracy (0.38 arcsec) is measured even including the aforementioned $z = 6$ structure using the spectroscopically confirmed and/or robust photometric redshifts objects not utilized by Caminha et al. (2017a) at the time the lens model was constructed. This highlights the excellent predicting power and the reliability of the model on 27 multiple images in total (9 individual objects at $z \simeq 6$ not shown here, Vanzella et al., in preparation).

As already discussed in Vanzella et al. (2017b), we probe extremely small physical sizes in the $z = 6.143$ system, exploiting the maximum magnification component, which is along the tangential direction in this case, as apparent from arc-like shape of the Ly α emission (see Fig. 1). Table 1 reports the total, μ_{tot} , and tangential, μ_{tang} , magnifications at the positions of D1. They are fully consistent with the previous estimates, but the uncertainties are now decreased thanks to the additional constraints discussed above. Statistical errors are of the order of 5 per cent. To access systematic errors we rely on the extensive simulations reported by Meneghetti et al. (2017), aimed at performing an unbiased comparison among different lens modelling techniques specifically applied to the Hubble Frontier Field project⁴ (including the code LENSTOOL used by Caminha et al. 2017a). In particular, the accuracy in reproducing the positions of multiple images (e.g. rms) correlates with the total error on magnification, especially at the position of the multiple images themselves (fig. 26 of Meneghetti et al. 2017). In the present case, considering the lens model adopted and the accuracy in reproducing the positions of the multiple images, the expected systematic uncertainty on the magnification factors is not larger than 30 per cent. This translates to a 1σ error for the magnification on D1 of $\mu_{\text{tot}} = 17.4 \pm 1_{\text{stat}} \pm 5_{\text{sys}}$, and for the tangential magnification, $\mu_{\text{tang}} = 13.2 \pm 0.5_{\text{stat}} \pm 4_{\text{sys}}$. The same arguments apply to the other compact source T1, for which we have $\mu_{\text{tot}} = 24 \pm 2_{\text{stat}} \pm 7_{\text{sys}}$, and $\mu_{\text{tang}} = 18 \pm 1_{\text{stat}} \pm 5_{\text{sys}}$ (see Table 1).

Table 1. The inferred physical, morphological, and lensing properties of D1 and its compact SF region (core). Also the properties of the local dwarf galaxy NGV 1705 are reported.

Quantity	Best value	Uncertainty
μ_{tot} (magnif.)	17.4	$\pm 1_{\text{stat}} \pm 5_{\text{sys}}$
μ_{tang} (magnif.)	13.2	$\pm 0.5_{\text{stat}} \pm 4_{\text{sys}}$
D1(total)		
$M(\text{stellar}) [\times 10^8 M_{\odot}] 1\sigma$	$3.8 \mu_{\text{tot}}^{-1}$	$[3.7-5.8] \mu_{\text{tot}}^{-1}$
$M(\text{stellar}) [\times 10^8 M_{\odot}] 3\sigma$		$[1.0-250] \mu_{\text{tot}}^{-1}$
Age [Myr] 1σ	1.4	[1–3]
Age [Myr] 3σ		[1–708]
SFR [$M_{\odot} \text{ yr}^{-1}$] 1σ	$275 \mu_{\text{tot}}^{-1}$	$[131-585] \mu_{\text{tot}}^{-1}$
SFR [$M_{\odot} \text{ yr}^{-1}$] 3σ		$[1-1350] \mu_{\text{tot}}^{-1}$
$E(B-V) 1\sigma$	0.15	[0.15–0.20]
$E(B-V) 3\sigma$		[0.0–0.30]
$m(1500 \text{ \AA})$ (intrinsic)	29.60	± 0.2
$M_{\text{UV}}(1500)$	–17.13	± 0.2
$\log(\Sigma_{\text{SFR}})^a$	1.39	[0.80–1.85]
R_e tang [pixel(pc)]	$3.4(44)^b$	$\pm 1.5(\pm 19)$
Half-size tang [pixel(pc)]	$17(220)^b$	$\pm 3(\pm 35)$
D1(core)		
Comment		
$M(\text{stellar}) [\times 10^7 M_{\odot}] 1\sigma$	$\simeq 1.5 \mu_{\text{tot}}^{-1}$	–
$m(1500 \text{ \AA})$ (intrinsic)	31.10	± 0.3
$M_{\text{UV}}(1500)$	–15.6	± 0.3
$\log(\Sigma_{\text{SFR}})^a$	> 2.5	$R_e < 26 \text{ pc (2 px)}$
$\log(\Sigma_{\text{SFR}})^a$	> 2.9	$R_e < 13 \text{ pc (1 px)}$
R_e tang [pixel(pc)]	$< 1.0(13)^b$	PSF shape
NGC1705 and SSC		
$M_{\text{UV}}(2000)(\text{NGC}1705)$	–17.3	± 0.1
$M_{\text{UV}}(2000)(\text{SSC})$	–15.2	± 0.1
$\log(\Sigma_{\text{SFR}})^a(\text{SSC})$	> 2.6	
R_e [pc]	4.0	F555W band

Note. ^a Σ_{SFR} in units of $M_{\odot} \text{ yr}^{-1} \text{ kpc}^{-2}$.

^b $R_e[\text{pc}] = R_e[\text{pixel}] \times 0.03 \text{ arcsec} \times 5660 \text{ pc}/\mu_{\text{tang}}$; 1 pixel = 0.03 arcsec; 1 arcsec = 5660 pc at $z = 6.14$.

2.2 The ultraviolet morphology of D1

Vanzella et al. (2017b) modelled the morphology of D1 using GALFIT (Peng et al. 2002, 2010). An approximate solution with Sersic index 3.0, $R_e \simeq 140 \text{ pc}$ ($\simeq 8 \text{ pixel}$, along the tangential direction), $q (= b/a) \simeq 0.2$, and a PA of -28.5 deg was found. However, we also noticed a prominent and nucleated core suggesting that a much compact emitting region is present. Subsequently, Bouwens et al. (2018) made use of the HFF observations to study extremely small objects with a scale of a few ten parsec. D1 was part of their sample, for which they estimate an effective radius of $38_{-14}^{+21} \text{ pc}$ (corresponding roughly to 3 pixel along maximum magnification). Here, we reanalysed in detail the morphology of D1.

2.2.1 Empirical half-light radius

We estimated the half-light radius in the F105W band that is the bluest band (with the narrowest PSF among the near-infrared ones) probing the stellar continuum redward the Ly α emission (see Fig. 3). While along the radial direction the profile is consistent with the PSF (FWHM = 0.18 arcsec, or 6 pixel), the tangential profile shows a resolved structure, with a prominent peak containing a large frac-

⁴<https://archive.stsci.edu/prepds/frontier/lensmodels/>

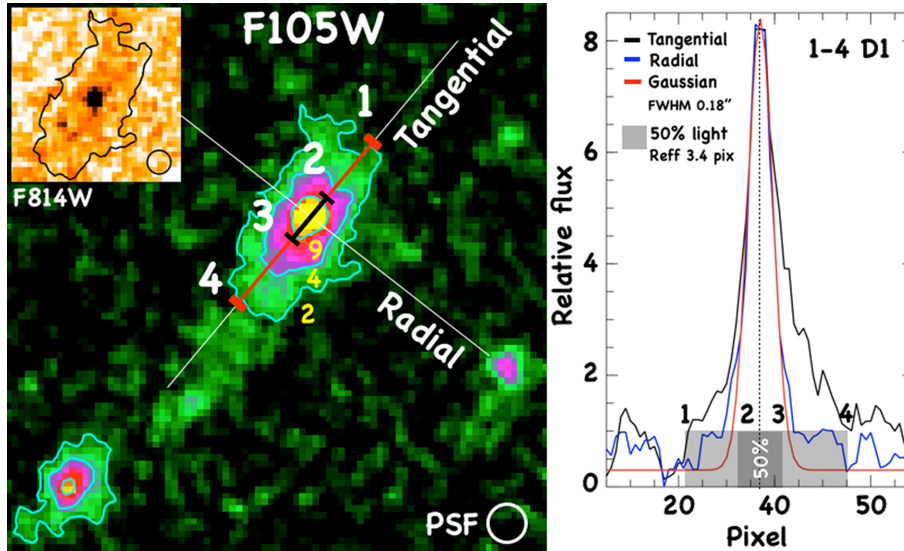


Figure 3. The tangential and radial profiles (labelled) extracted from the $F105W$ band and centred on the core of D1 are shown in the right-hand panel. The Gaussian shape with FWHM of 0.18 arcsec (equal to the width of the PSF, or 6 pixel) is also superimposed with a red line and is consistent with the plotted radial profile (as expected given the modest radial magnification, $\mu_R \simeq 1.3$). The 50 per cent of the light along the tangential direction (marked with the segments 1–4 in the left-hand panel) is enclosed within ~ 9 pixel (segments 2–3) and shown with a grey stripe, corresponding to a PSF-corrected size of ~ 6.8 pixel (and a radius of 3.4 pixel or $R_c \simeq 44$ pc). In the left-hand panel, the $F105W$ image of D1 and T1 is shown, in which the cyan contours mark the 2σ , 4σ , and 9σ levels above the background. The PSF size is also shown with a white circle (0.18 arcsec diameter). In the top-left inset the $F814W$ image of D1 is also shown with the same 9σ contour based on the $F105W$ band. The presence of the IGM in the $F814W$ band attenuates the signal that, however, still reveals a nucleated emission (compatible with the $F814W$ PSF, FWHM = 0.16 arcsec).

tion of the UV light. In particular, the observed (one-dimensional) 50 per cent of the light is enclosed within $\simeq 9$ pixel, suggesting a radius of $\simeq 4.5$ pixel (not PSF-corrected). If corrected for the PSF-broadening (one-dimensional) the empirical half-light radius is 3.4 pixel, that at the redshift of the source ($z = 6.143$) and $\mu_{\text{tang}} = 13.2$, corresponds to $\simeq 44$ parsec (in agreement with Bouwens et al. 2018). Looking more into the details, the inner region of D1 shows a circular symmetric shape despite the large tangential stretch (see e.g. contours in Fig. 3), suggesting a quite nucleated entity significantly contributing to the UV light (reported below) on top of a more extended *envelope* or dwarf (dubbed D1). In the following we refer to this compact region as D1(core). The same highly nucleated region is also evident in the ACS/ $F814W$ band, whose PSF (0.16 arcsec) is slightly narrower than the WFC3/ $F105W$. Though the intergalactic medium transmission affects half of the $F814W$ band and depress significantly the overall signal, the S/N of D1(core) is high enough ($S/N \simeq 6$) to still appreciate its compactness (Fig. 5) and, again, well reproduced with a pure *HST* PSF. In the next section, we perform specific simulations to quantify the size of D1 and its core.

2.2.2 GALFIT modelling

No satisfactory solution can be obtained from a GALFIT PSF deconvolution of D1 by adopting a single component [i.e. a single Sersic index, ellipticity $q(=b/a)$, position angle (PA), and effective radius (R_e) parameters], mainly due to the steep gradient towards the central region. This reflects the fact that the core appears spatially unresolved, requiring at least two components. Indeed, a very good model is obtained combining a Gaussian extended shape that reproduces the diffuse envelope surrounding the core, and a superimposed PSF-like profile which reproduces the central emission (as described in detail in the next sections). Fig. 4 shows the two-component GALFIT modelling and residuals after subtracting the

model from the observed $F105W$ -band image (for both D1 and T1 objects). In the following, we focus on the detailed analysis of the size, and eventually the nature, of the nuclear region of D1. It is worth noting that D1 offers a unique opportunity to access such a nucleated region down to an unprecedented tiny size for three reasons: (1) it lies in a strongly gravitationally amplified region of the sky ($\mu_{\text{tang}} > 10$), (2) the emitting core is boosted (in terms of S/N) by the underlying well detected envelope (or dwarf), which also implies (3) that the detection of the underlying envelope guarantees the full light of the core is captured. In the next section, the shape of the core is specifically addressed.

2.2.3 The core of D1: a source confined within 13 parsec

Depending on the S/N of object and on the knowledge of the PSF, a sub-pixel solution for R_c (after PSF deconvolution) can be typically achieved with GALFIT (e.g. Peng et al. 2010; Vanzella et al. 2016b), as also explored with dedicated simulations (e.g. Vanzella et al. 2017b), especially in relatively simple objects showing circular symmetric shapes like the present case. The central part of D1 is very well detected in all the WFC3/NIR bands, in particular in the $F105W$ band with an $S/N \gtrsim 50$ calculated within a circular aperture of 0.18 arcsec diameter. We adopted two PSFs in the simulations: (1) one extracted from an extensive and dedicated work by Anderson (2016) and (2) a PSF extracted by averaging three non-saturated stars present in the same field of the target. The former method benefits from large statistics and accurate monitoring of the spatial variation along the CCD, the latter includes the same reduction process also applied to the target D1. The model PSF from Anderson in the $F105W$ band is slightly narrower (FWHM $\simeq 0.16$ arcsec) than the PSF extracted from the stars in the field (FWHM $\simeq 0.18$ arcsec). Both PSFs are useful to monitor the systematic effects in recovering the structural parameters as discussed

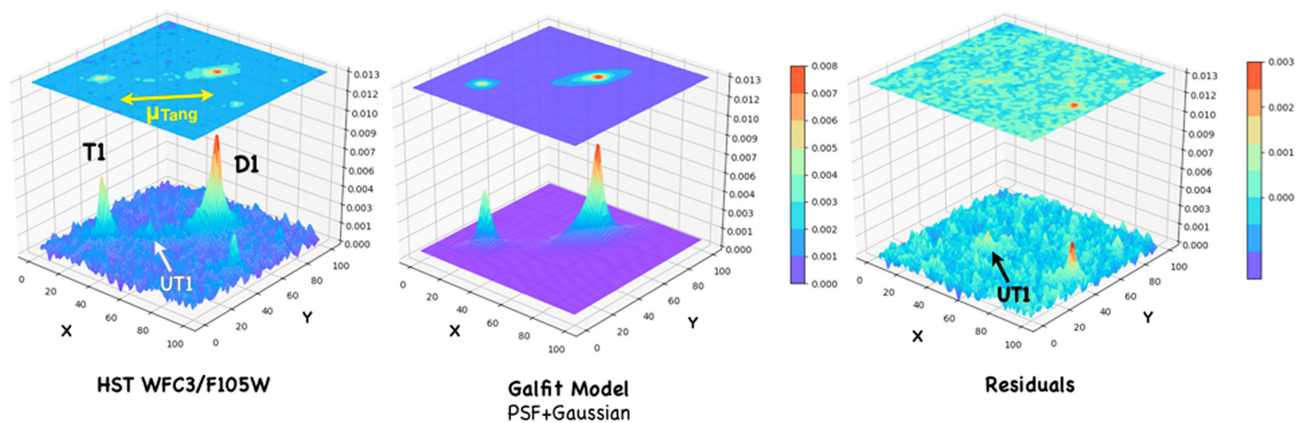


Figure 4. GALFIT modelling in the $F105W$ band. The best model includes two components: a diffuse Gaussian component well reproducing the extended envelope with superimposed a pure PSF that well reproduces the morphology of the core. From left to right: the *HST* original images, the GALFIT model, and the residuals (i.e. the difference of the two quantities) are shown in the pixel domain in the XY -plane and colour-coded in the Z -axis following the HFF/WFC3 counts in the $F105W$ band.

in Appendix A. In the following, we adopt the PSF extracted from the stars present in the same image.

The same procedure described in Vanzella et al. (2016a, 2017b) is adopted, where we run GALFIT on a grid of key parameters like R_e , magnitude, and Sersic index n , after fixing the PA, the ellipticity ($q = b/a$), and the coordinates of the core (X, Y). These fixed parameters are easily determined a priori, especially for objects like the core of D1: circular symmetric and nearly PSF-like (e.g. by running GALFIT leaving them free at the first iteration). At each step (i.e. moving in the grid of the parameter space along R_e , n , and magnitude, with step 0.1, 0.25, and 0.1, respectively) the various statistical indicators (standard deviation, mean, median, min/max values) have been calculated in a box of 8×8 pixel ($0.24 \text{ arcsec} \times 0.24 \text{ arcsec}$) centred on D1(core) (see Fig. 5). The standard deviation and the median signal within the same box calculated in the ‘observed-model’ image (image of residuals) are monitored. At a given n , the smallest standard deviation is reached at the smallest radii, when the residual signal approaches the mean value of the underlying, more extended envelope. This is shown in Fig. 5 in which five snapshots of the residuals on D1(core) at decreasing radii are included. The core is very well subtracted using a model with $n = 0.5$ (Gaussian shape), magnitude 28.0 and R_e smaller than 1 pixel. The same figure shows the standard deviation as a function of R_e , in which the monotonically decreasing behaviour without a clear minimum indicates that sub-pixel solutions are preferred. It is also worth noting that the case of $R_e = 1$ pixel still leaves a positive residual suggesting that sub-pixel R_e better matches the D1(core) (Fig. 5). Dedicated simulations on mock images quantitatively support this result and provide an upper limit on R_e at sub-pixel scale (see Appendix A).

In particular, Fig. 5 and the simulations described in Appendix A (given the S/N and the relatively simple circular symmetric shape) imply that in principle, it is possible to resolve D1(core) down to $R_e = 1$ pixel. Conversely, D1(core) is not resolved, however, we can provide a plausible upper limit lower than 1 pixel (noting that the cases with $R_e = 0.75$ pixel are also recognized in the simulations, though with a less success rate, see Figs 5 and A1, red curve). These limits (0.75/1.0 pixel) corresponds to radii $R_e < 10\text{--}13$ pc at $z = 6.143$, along the tangential direction discussed above. A size smaller than 2 pixel (26 pc) would be a very conservative choice.

It is worth noting that the 25 per cent of the UV emission of D1 (the entire dwarf) is confined within such a small size [D1(core)], suggesting a remarkably dense star formation rate surface density in that region, as discussed in the next section.

2.3 Physical properties of D1

SED-fitting of D1, based on the Astrodeep photometry (Merlin et al. 2016) and using nebular prescription (Castellano et al. 2016) coupled to Bruzual & Charlot (2003) models, was presented in Vanzella et al. (2017b) and is shown in the left-hand panel of Fig. 6. Here we briefly summarize the results, extend the analysis on the degeneracies among the most relevant parameters, thus inferring the basic properties of D1(core). Thanks to the amplification due to gravitational lensing, the faint intrinsic magnitude of D1 (29.60) is placed in a bright regime (magnitude $\simeq 26.5$) with $\Delta m = -2.5 \text{Log}_{10}(\mu_{\text{tot}}) = 3.1$ ($\mu_{\text{tot}} = 17.4$). Given the depth of the HFF data, the resulting S/N is larger than 20 in all the *HST*/WFC3 bands (from Y to H bands). As discussed in Vanzella et al. (2017b), the relatively small photometric error in the VLT/HAWKI K_s -band ($S/N \simeq 3.5$) leads to non-degenerate solutions (within 1σ) among SFR, stellar mass, and age. Table 1 summarizes the best-fitting values with the 1σ and 3σ intervals. The solutions at 1σ , 2σ , and 3σ are also shown in Fig. 7, in which the degeneracy among the stellar mass, age, and star formation rate is evident when relaxing to 3σ , mainly due to the lack of constraints at optical rest-frame wavelengths. Since the distribution of the SFR changes significantly from 68 per cent(1σ) to 99.7 per cent(3σ) intervals, we conservatively adopt the 3σ distribution for the following calculations. In the next section, we will provide additional constraints on the SFR and the age of the system by considering the $\text{Ly}\alpha$ emission.

2.3.1 Additional constraints from $\text{Ly}\alpha$ emission

Prominent $\text{Ly}\alpha$ emission emerging from the DIT1 complex has been detected in all the three multiple images covered by the VLT/MUSE, and follows a well-developed arc-like shape (Fig. 8, see also Caminha et al. 2017a; Vanzella et al. 2017b). We calculate the rest-frame equivalent width of the $\text{Ly}\alpha$ line [$\text{EW}_{\text{rest}}(\text{Ly}\alpha)$] by integrating the

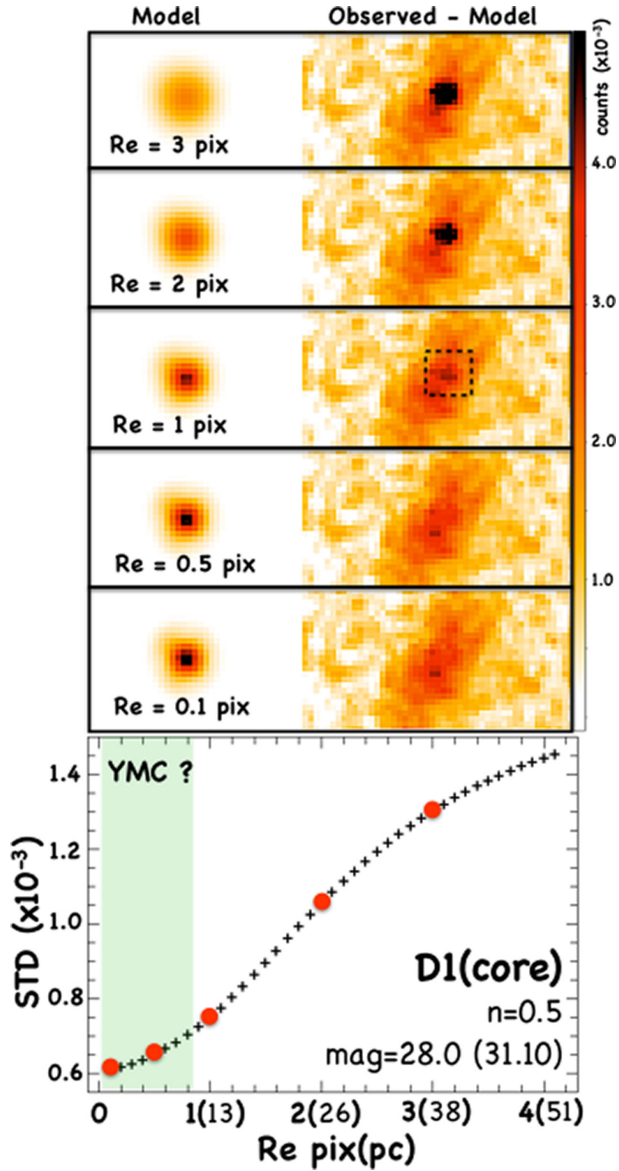


Figure 5. A detail of the GALFIT modelling of the D1 nuclear emission in the $F105W$ band. The five images on the top show the models and residuals (observed – model) for various values of the effective radius (R_e). At $R_e = 1$ pixel the residual is still positive, suggesting the object has an $R_e < 1$ pixel (see the text for details). In the bottom panel, the behaviour of the standard deviation (calculated at each step within the area outlined with the dotted box shown in the panel at $R_e = 1$ pixel) is shown with a finer grid of R_e (at fixed $n = 0.5$ and magnitude 28), and shows a monotonically decreasing shape never reaching a minimum, suggesting that (at given the S/N ratio) the intrinsic size is not recovered and lies below the deconvolution capabilities of the algorithm, implying an $R_e < 1(13)$ pixel(pc). Filled red circles mark the five cases reported in the top images, $R_e = 3, 2, 1, 0.5$, and 0.1 pixel. The green shaded area on the bottom marks the typical R_e of YMCs observed locally.

$\text{Ly}\alpha$ flux and the UV continuum over the same apertures. Two estimates of the $\text{EW}_{\text{rest}}(\text{Ly}\alpha)$ have been derived adopting two apertures: a *local* aperture that brackets the system D1T1 (see the elliptical magenta aperture in Fig. 8) and a *global* aperture that includes the entire $\text{Ly}\alpha$ flux (the yellow 3σ contour in Fig. 8). The observed line

flux for the local(global) aperture is $2.5(6.7) \times 10^{-17} \text{ erg s}^{-1} \text{ cm}^{-2}$ (with an error smaller than 10 per cent) and the magnitude of the continuum at the $\text{Ly}\alpha$ wavelength ($\lambda = 8685 \text{ \AA}$) has been inferred summing up the emission arising from the full system D1T1, $m \simeq 26.0$. Within the 3σ contour $\text{Ly}\alpha$ arc, no evident *HST* counterparts have been identified, besides the D1T1 complex, suggesting that the bulk of the ionizing radiation producing the $\text{Ly}\alpha$ arc is generated by this system.⁵ The magnitude of the continuum has also been corrected for the observed UV slope ($\beta = -2.5$; Vanzella et al. 2017b). The resulting rest-frame $\text{EW}_{\text{rest}}(\text{Ly}\alpha)$ is 60 ± 8 and $161 \pm 15 \text{ \AA}$ for the local and global apertures, respectively. While these are large values that place complex D1T1 in the realm of $\text{Ly}\alpha$ emitters, the intrinsic EW is plausibly higher than the observed one, for mainly two reasons: (1) the clear asymmetry of the line profile suggests the bluer part of the line is undergoing radiative transfer effects, being possibly attenuated by the intergalactic, circumgalactic, and/or the interstellar H I gas. A factor two attenuation is a conservative assumption at these redshifts (Laursen, Sommer-Larsen & Razoumov 2011; de Barros et al. 2017) and (2) the best SED-fit allows for the presence of low or moderate dust attenuation, in the range $E(B - V)_{\text{stellar}} \simeq 0.0 - 0.15$ that would make the observed line flux a lower limit. Given the resonant nature of the $\text{Ly}\alpha$ transition that make such a line fragile when dust is present and the fact that the dust attenuation would be typically larger for the nebular lines than the stellar continuum (e.g. Calzetti et al. 2000; Hayes et al. 2011), the intrinsic equivalent width of the line is likely higher than observed. The current data prevent us from quantifying the dust attenuation (future observations of the Balmer lines with *JWST* will provide valuable hints on that), therefore we consider the H I attenuation only (case 1) and assume no dust absorption, i.e. the inferred EWs are still lower limits due to the possible presence of (even a small amount of) dust. Therefore, plausible lower limits on the equivalent widths are $\text{EW}_{\text{rest}}(\text{Ly}\alpha) > 120$ and $> 320 \text{ \AA}$ for the local and global apertures, respectively. The presence of such a copious $\text{Ly}\alpha$ emission implies an ionization field associated with young stellar populations. Indeed, even in the most conservative case [$\text{EW}_{\text{rest}}(\text{Ly}\alpha) > 60(120) \text{ \AA}$], the comparison with the temporal evolution of the $\text{Ly}\alpha$ equivalent width extracted from synthesis models suggest an age of the star-forming region(s) younger than 100 Myr, or even younger than 5 Myr in the case of bursty star formation. Fig. 8 shows the $\text{EW}_{\text{rest}}(\text{Ly}\alpha)$ as a function of the age, metallicity, instantaneous burst, and constant star formation extracted from models of Schaerer (2002). The observed $\text{Ly}\alpha$ luminosity also provides a lower limit on the star formation rate, assuming the case B recombination applies here (Kennicutt 1998a). The observed $\text{Ly}\alpha$ luminosity for D1T1 is $1.05 \pm 0.05 \times 10^{43} \text{ erg s}^{-1}$ (derived from the local aperture accounting for the factor 2 due to H I attenuation, see the case (1) above) and corresponds to $\text{SFR} > 20(51) M_{\odot} \text{ yr}^{-1}$, in the case of local (or global) aperture (Fig. 8). Since we are focusing on the D1 source only, a very conservative lower limit of $\text{SFR} > 6 M_{\odot} \text{ yr}^{-1}$ has been calculated by integrating the $\text{Ly}\alpha$ flux within a circular aperture of 1 arcsec diameter centred on D1. Fig. 7 shows the 1σ , 2σ , and 3σ solutions of the SED-fitting for D1 including the aforementioned constraints inferred from the $\text{Ly}\alpha$ emission (orange arrows).

⁵Possible additional fainter sources of ionizing radiation may contribute to the total $\text{Ly}\alpha$ flux, however, they would be more than 2.5–3.0 mag fainter than D1 and T1, and consequently their contribution would be negligible in our analysis. The $F105W$ magnitude of the D1T1 star-forming complex has been derived from the Astrodeep photometry.

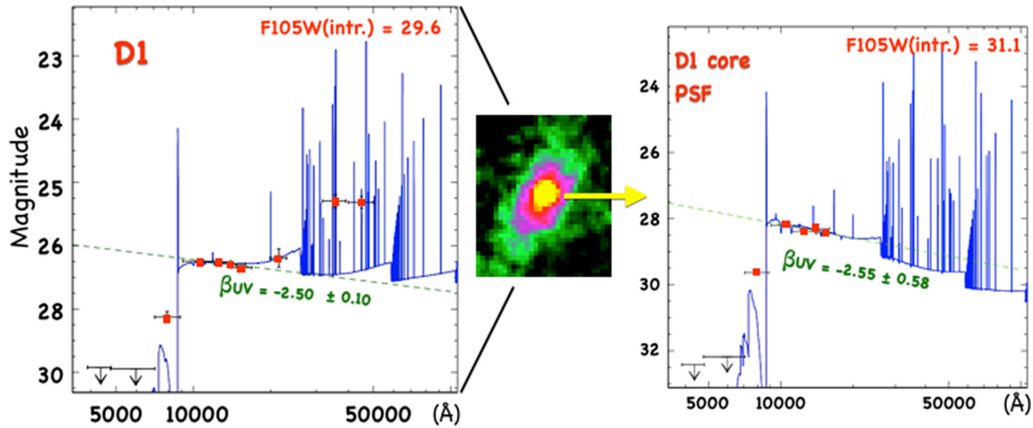


Figure 6. The best SED-fit solutions for D1 (left) and for the core of D1 (right) are shown. Only the *HST* photometry is shown for the core and no VLT/*Ks*-band or *Spitzer*/IRAC magnitudes have been extracted. This comparison shows a first-order consistency among the core and the full D1 object, for which very similar ultraviolet slopes (β_{UV}) are derived. In the middle, the *F105W* image of D1 and its core (highlighted in yellow) are shown.

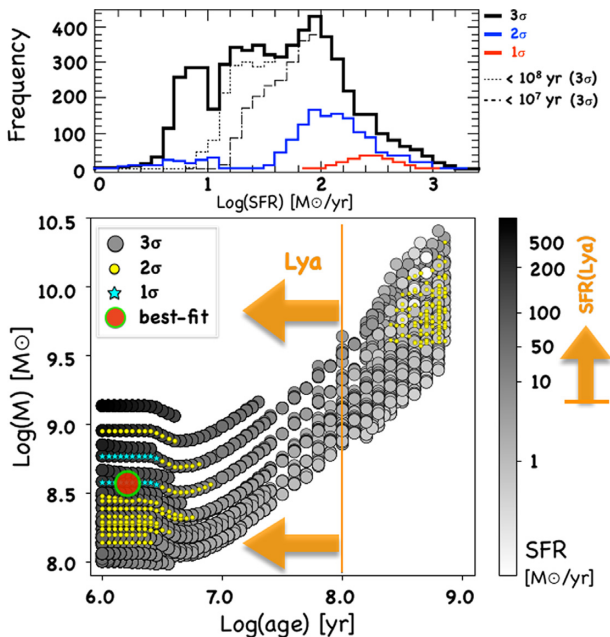


Figure 7. *Bottom:* The 3σ solutions (99.7 per cent) derived from the SED-fitting of D1 as a function of the stellar mass, age, and star formation rate (grey-coded circles). The 2σ and 1σ solutions are shown with yellow dots and cyan stars, respectively. Solutions with ages younger than 100 Myr and favoured by the $\text{Ly}\alpha$ equivalent width are indicated with the orange arrows, along with the minimum SFR inferred from the $\text{Ly}\alpha$ luminosity. The filled red circle marks the position of the best-fitting solution, for which the best model is shown in Fig. 6. *Top:* The distribution of the star formation rates calculated within (3, 2, 1) σ is shown for D1. Distributions at 3σ with ages younger than 100 and 10 Myr are also shown with long-dashed and dotted lines. The distribution at 3σ with age younger than 100 Myr has been used in the MC calculations for the estimate of the Σ_{SFR} , see Section 2.3.2.

2.3.2 A superdense star-forming region hosted by the dwarf galaxy D1

The prominent and nucleated UV emission arising from the core of D1 suggests a particularly high star formation rate surface density (SFRSD or Σ_{SFR} hereafter, [$\text{M}_{\odot} \text{yr}^{-1} \text{kpc}^{-2}$]) which we derive using a Monte Carlo approach that includes the uncertainties of all relevant parameters.

(i) *The ultraviolet size.* As discussed in Section 2.2.3, in the following calculations we consider 1 pixel (13 pc) as an upper limit for the effective radius of the nuclear region. It is worth anticipating, however, that even adopting a more conservative assumption of $R_e = 2$ pixel (26 pc), the resulting Σ_{SFR} still lies in the high-density regime (see below).

(ii) *The star formation rate.* Fig. 6 shows the best SED-fit solutions for D1 and D1(core). In the latter case, the aperture photometry matching the *HST* PSF (0.18 arcsec diameter) has been specifically performed. Given the lower spatial resolution (respect to *HST*), the VLT/*Ks* and the *Spitzer*/IRAC bands have not been considered in the fit. The critical condition in which the photometric analysis is performed (very localized region) and the faintness of the object ($m \simeq 28$) prevent us from deriving solid results from the SED-fit procedure directly, that simply mirrors the same degeneracies we see for D1 at 3σ , but here at 1σ for D1(core). We therefore adopt the SFR derived for D1 (whose SED-fit benefits from a much brighter photometry) and rescale it accordingly to the flux density ratio in the ultraviolet. Specifically, both objects show a fully consistent spectral shape (Fig. 6), as steep as $\beta \simeq -2.5$ [-2.50 ± 0.10 and -2.55 ± 0.58 for D1 and D1(core), respectively]. Given this photometric similarity, the co-spatiality and the $\text{Ly}\alpha$ emission suggesting a relatively short age of the burst, It is reasonable to assume that they shared a common SFH; in this case, a good proxy for the SFR of the core can be obtained by rescaling the SFR of D1 by the measured ultraviolet luminosity density ratio among the two, i.e. we adopt proportionality among the ultraviolet luminosity and the SFR (Kennicutt 1998a), such that $L_{1500}(\text{core})/L_{1500}(\text{D1}) \simeq \text{SFR}(\text{core})/\text{SFR}(\text{D1}) \simeq 0.25$, L_{1500} is derived from the *F105W* band on the basis of the morphological analysis discussed above. We assume the uncertainty of the flux ratio follows a Gaussian distribution with $\sigma = 0.04$, given by the flux error propagation (used in the MC calculation). We note that the SFR inferred from the SED-fitting directly performed on D1(core) spans the 68 per cent interval of $1\text{--}40 \text{ M}_{\odot} \text{yr}^{-1}$ (i.e. $0.06\text{--}2 \text{ M}_{\odot} \text{yr}^{-1}$ intrinsic, see Appendix B), similar to what obtained by rescaling the global fit of D1 as mentioned above. The stellar mass inferred for D1(core) is $1.5 \times 10^7 \text{ M}_{\odot}$, i.e. $\simeq 0.86 \times 10^6 \text{ M}_{\odot}$ intrinsic (see Table 1, with the usual caveats related to the limited spectral coverage, see Section 5.1). Therefore, the stellar mass of D1(core) is $\lesssim 10^6 \text{ M}_{\odot}$ (Appendix B).

From three key quantities, i.e. magnification, morphology, and the SFR, we derive the Σ_{SFR} of the two objects, D1 and D1(core).

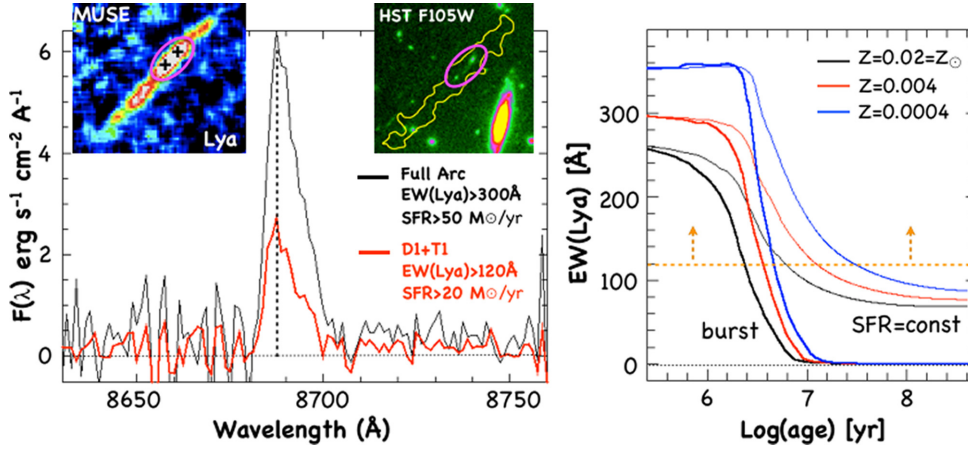


Figure 8. *Left:* The Ly α emission of the system DIT1 extracted from two apertures in the MUSE datacube: *local* (magenta ellipse in the top-left inset, red spectrum) and *global* including the full arc (yellow contour in the top-right inset, $>3\sigma$, black spectrum). The black crosses in the top-left inset mark the position of D1 and T1 on the Ly α arc. The top-right inset shows the same region in the HST WFC3/F105W band along with the Ly α contour (yellow line) and the magenta aperture, from which the Ly α and UV continuum have been measured to derive the Ly α equivalent width (see the text for details). *Right:* The evolution of the Ly α equivalent width as a function of time for different star formation histories and different metallicities, computed with the Schaerer (2002) models, assuming a Salpeter (1955) IMF and upper mass limit of 100 M_{\odot} . The horizontal orange dashed line with arrows marks the lower limit on the Ly α equivalent width inferred for the system DIT1 ($>120 \text{ \AA}$).

The size of D1 has been inferred from the *F105W* band and corresponds to 17 ± 3 pixel (corresponding to 0.5 arcsec observed, or 220 ± 38 pc in the source plane along the tangential direction). The size of the core is spatially unresolved with an effective radius less than 13 pc in the source plane and along the tangential direction. The SFR distribution within the 3σ interval has been considered after selecting those solutions associated with an age younger than 100 Myr, as inferred from the Ly α equivalent width (see Figs 7 and 8).⁶ The SFRSD has been calculated by extracting 10 000 values for the tangential magnification μ_{tang} , ultraviolet sizes, and the SFRs, accordingly with best estimates/limits and uncertainties. In particular, μ_{tang} is assumed to follow a Gaussian distribution with mean 13.2 and $\sigma = 4.0$ (see Section 2.1). The size of D1 is drawn from a Gaussian distribution with mean 17 pixels and $\sigma = 3.0$ pixels (see 2σ contour shown in Fig. 3), while in the case of D1(core) the effective radius of 1(2) pixel [or 13(26) pc] is assumed as an upper limit for the size (the 2 pixel as a very conservative assumption). The SFR has been randomly extracted from 3σ distributions resulting from the SED-fitting as discussed above. While the magnification and the sizes are robustly estimated, the SFR is the most uncertain and degenerate parameter (with age, stellar mass, and metallicity), for this reason we relax the interval within which the SFR is drawn, thus including also the lower tail of SFRs and less dense solution (see 1σ , 2σ , and 3σ histograms in Fig. 7). The same Monte Carlo approach was used to compute the Σ_{SFR} of T1, part of the same star-forming complex. The results are shown in Fig. 9, in which the Σ_{SFR} of T1, D1, and D1(core) are reported in the context of the KS law (Kennicutt 1998b), noting that currently no information is available for what concerns the gas surface densities (an approved ALMA program is ongoing and includes the DIT1 system, PI: Calura).

While D1 shows a moderate SFRSD, i.e. $\text{Log}_{10}(\Sigma_{\text{SFR}})_{\text{D1}} = 1.39^{+0.55}_{-0.56}$, the same quantity for D1(core) and T1 are quite large, $\text{Log}_{10}(\Sigma_{\text{SFR}})_{\text{core}} > 2.5$ and $2.7^{+0.5}_{-0.4}$, respectively. It is worth noting that Σ_{SFR} for D1 and T1 might represent an upper limit if the true

sizes are underestimated, whereas Σ_{SFR} of D1(core) should be regarded as a lower limit, as this object is spatially unresolved and well captured over the underlying more diffuse stellar continuum (see Section 2.2). In particular, the lower limit derived for the core is 2.9 in the case of $R_e < 1$ pixel (13 pc), and 2.5 if relaxed to the conservative value of $R_e < 2$ pixel (26 pc). We recall that the above values have been calculated selecting the solutions of the SED-fit with ages younger than 100 Myr (as Ly α properties suggest, see Section 2.3.1 and Fig. 7, top panel), however, even including older ages (corresponding to lower SFR) the result does not change significantly.

3 SIMULATING STRONGLY LENSED LOCAL YMCS AT $z = 6$

We have assessed the reliability of the above analysis by performing end-to-end image simulations with the software SKYLENS (Meneghetti et al. 2008, 2010; Plazas et al. 2019) and following the same approach described in appendix A of Vanzella et al. (2017b). This code can be used to simulate observations with different instrumentation (e.g. HST, JWST, ELT), including the lensing effects produced by matter distributions along the line of sight to distant sources. Here, we consider the compact blue galaxy BCD NGC 1705 as a local proxy for D1, and place it in the source plane at $z = 6.143$ at the same position of the source that generates D1, and then lensed on the sky plane using the same model adopted in this work. NGC 1705 contains a relatively massive and young SSC of mass $7.15 \times 10^5 M_{\odot}$, with an age of 15 Myr and $R_e = 4$ pc (measured in the optical *F555W* band). About 10 more lower mass star clusters (10^4 – $10^5 M_{\odot}$) are present with typically older ages spanning the range (>10 –1000 Myr, Annibali et al. 2009). The absolute magnitudes of NGC 1705 galaxy and the SSC are $M_{\text{UV}} \simeq -17.3$ (Rifatto, Longo & Capaccioli 1995) and -15.2 (derived from HST/UV observation of the LEGUS survey; Calzetti et al. 2015), with a distance modulus of $(m-M) = 28.54$ (Tosi et al. 2001). These magnitudes are referred to $\lambda \simeq 2000 \text{ \AA}$, close to the rest-frame wavelength observed in the *F105W* band at $z = 6.143$, $\lambda \simeq 1500 \text{ \AA}$ (we do not apply any correction associated with the spectral

⁶The results do not change significantly if we include all the possible SFRs and impose a limit on the age equal to the age of the Universe at $z = 6.1$.

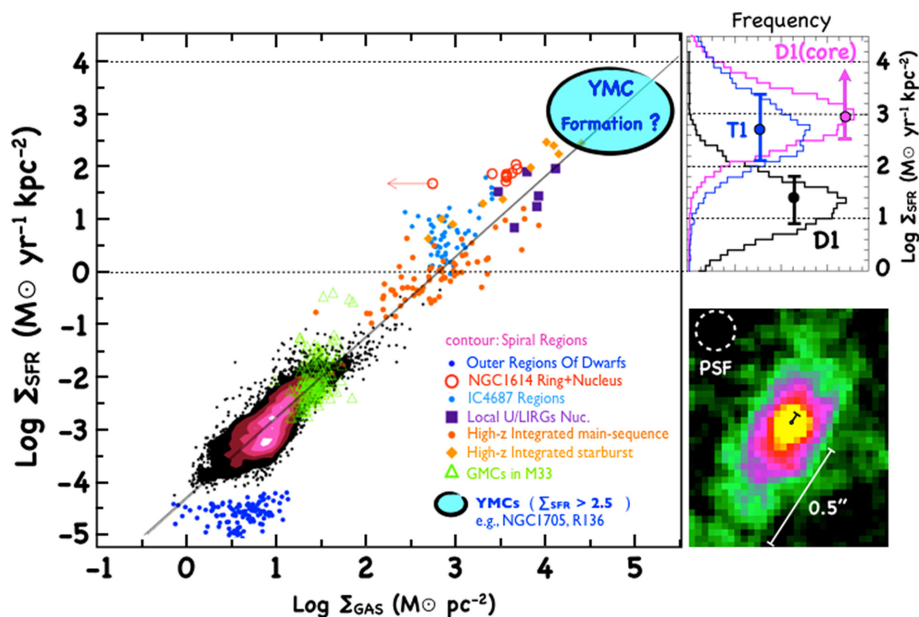


Figure 9. KS law from various estimates in the literature (adapted from Shi et al. 2018). The SFR surface density distributions for D1, D1(core), and T1 are shown in the top-right panel with black, magenta, and blue lines, respectively (see the text for details). The filled circles with 68 per cent central interval mark the medians of the corresponding distributions and are shifted in the X -direction for clarity. Note the magenta point corresponds to a lower limit. In the bottom-right panel, the $HST/F105W$ image of D1 is shown, in which the segments indicate the 26 pc physical size for the core (black line) and ~ 200 pc for D1 (white line). The dashed circle shows the PSF size in the same $F105W$ band (0.18 arcsec diameter).

slope). The estimated absolute magnitudes of D1 and D1(core) are -17.1 and -15.6 therefore quite close to the UV luminosities of NGC 1705 and its SSC.

The bluest band observed in the LEGUS survey (WFC3/ $F275W$) provides the image that we used as a model in our simulation, in which each pixel corresponds to 1 pc (0.0396 arcsec at 5.1 Mpc; Tosi et al. 2001). Fig. 10 (left-hand panel) shows the $F275W$ image of NGC 1705 and a zoomed region of the SSC, in which the SSC dominates the UV emission. We simulated HST observations by adding the modelled lensed dwarf to the $F105W$ HFF image (rescaled to the magnitude of D1 and reproducing an S/N consistent with the observed one), in four positions near the system D1T1 to facilitate a direct comparison with the real object (see Fig. 10). NGC 1705 is marginally recovered and slightly elongated along the tangential direction (as expected). A prominent and nucleated emission is evident and corresponds to the position of the SSC. We performed the same GALFIT fitting as applied for D1 on these four mock NGC 1705 images and find a satisfactory solution when the PSF was subtracted (as for D1, see top-right panel of Fig. 10). In practice, similarly to D1, the core of NGC 1705 is not resolved and an upper limit of $R_e = 13$ pc can be associated (in this case we know the SSC has a radius of 4 pc). It is clear from this test that the nucleated region of D1 appears consistent with a spatially unresolved SSC, as it emerges from NGC 1705. Another factor that limits the possibility to detect and/or spatially resolve single star clusters under such conditions is the large differential magnification along radial and tangential directions: two close SSCs aligned along radial direction cannot be distinguished, while along the tangential direction the current resolution does not allow us to probe single star clusters with radii smaller than 15 pc (at least in this specific case in which $\mu_{\text{tang}} \simeq 13$). As discussed in Section 5.1, a sizeable sample of candidate star clusters observed at higher spatial resolution will alleviate these limitations.

3.1 An E-ELT preview

A significant increase of the spatial resolution will be possible in the future by means of extremely large telescopes. Fig. 10 shows a simulation of the same lensed dwarf galaxy NGC 1705 performed considering the 40 m E-ELT. We specifically consider the expected PSF in the H band of the MICADO camera (Multi-AO Imaging Camera for Deep Observations) coupled with the MAORY module (Multi-conjugate Adaptive Optics RelaY) adopting the MCAO (Multi-Conjugate Adaptive Optics) and narrow field mode (0.0015 arcsec pix^{-1} and FWHM of $\simeq 10$ mas).⁷ The H and $F275W$ bands probe very similar rest-frame wavelengths, $\lambda = 2240 \text{ \AA}$ and $\lambda \sim 2700 \text{ \AA}$. As shown in Fig. 10, the pixel scale/resolution corresponds to 6.5/40 pc (radial) and 0.65/4 pc (tangential) in the specific case of the strongly lensed D1. The E-ELT PSF (0.01 arcsec), 18 times smaller than the one of HST in the H band, and the much larger collecting area lead to a dramatic increase of morphological details. The noise in the simulation is generated from a Poissonian distribution following the expected performances of the telescope and the MICADO + MAORY instruments. In particular, an $S/N \simeq 50$ is expected for a point-like object of $H = 25.6$ Vega ($\simeq 27$ AB) and 3 h integration time, within an aperture of 10×10 mas. From Section 2.2.3, the inferred magnitude of D1(core) is $\simeq 28$ (AB) and with the addition of the underlying dwarf (D1) the total observed magnitude is 27.25 (AB), or 25.85 Vega. Along the radial direction the expected profile is PSF dominated ($\mu_{\text{rad}} \sim 1$), while along tangential direction the resolution is sufficient to resolve NGC 1705 SSC-like objects, though they will still appear nucleated, as the R_e of the SSC and the resolution element, 10 mas, are similar ($\simeq 4$ pc). We therefore expect an S/N slightly lower than 50. Although the performances of MICADO, MAORY, and the telescope are still

⁷The nominal performances are reported at the following link: <http://www.aory.oabo.inaf.it/index.php/science-pub/>.

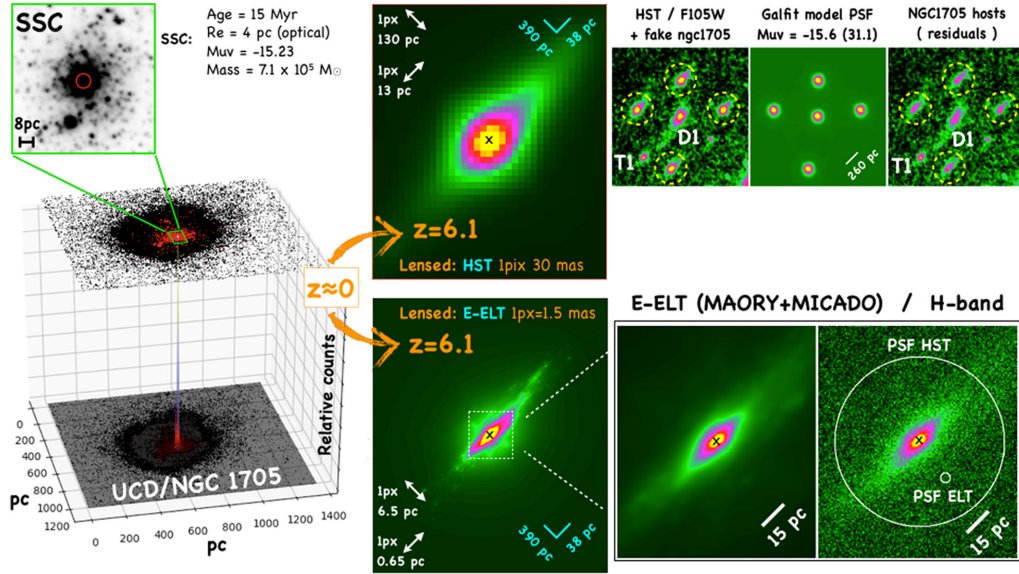


Figure 10. SKYLENS simulation of the ultracompact dwarf galaxy NGC 1705 hosting its SSC. In the left-hand panels, the WFC3/*F275W* image of the galaxy is shown in 3D and 2D with highlighted the prominent UV emission of the SSC (top-left inset). The main properties of the SSC are also reported. In the top-right panels (from left to right): the modelled noiseless dwarf at the *HST* resolution lensed at $z = 6.143$ in the *F105W* band (the pixel scales are indicated along radial/tangential directions); the same model added to the *F105W* image in four positions (dashed yellow circles); the GALFIT models of the core of NGC 1705 (see the text for details); the subtracted PSF models of the previous two images, showing the unresolved core of the dwarf dominated by the SSC (the position of the SSC is marked with a black cross in the modelled image). In the bottom panels, the same simulation is shown adopting the MAORY + MICADO PSF in the MCAO narrow field mode. The bottom-right panels show the zoomed region in which the physical scale and the two PSFs (*HST* and MICADO + MAORY) are indicated.

under definition, it is reasonable to expect an S/N for D1(core) in the range $30 < S/N < 70$ with a few hours integration time, sufficient to measure the real size of the star cluster. Fig. 10 shows that, depending on the local magnification, an SSC at $z \sim 6$ will likely be resolved along the tangential direction, as the effective radius will be sampled with a resolution element of 4 pc (10 mas). A proper PSF deconvolution (as performed in this work) should allow to spatially resolve the light profile of the star clusters ($R_e \simeq 4$ pc), in which 1 pixel corresponds to $\simeq 0.65$ pc. Possible fainter unresolved substructures will also emerge, allowing a proper photometric and spectroscopic analysis of the SSC (i.e. with significantly reduced confusion).

4 DISCUSSION

4.1 A possible young massive star cluster hosted by D1

Star clusters are cradles of star formation and grow within giant molecular clouds (GCM)-large collections of turbulent molecular gas and dust, with masses of $10^{4-7} M_\odot$ and with typical sizes of 10–200 pc. Previous studies have shown that in the local Universe the fraction of star formation occurring in bound star clusters – usually referred to as the cluster formation efficiency Γ (Bastian 2008) – increases with the SFRSD of the star-forming complexes or galaxies hosting such clusters. This emerges from observations of a sample of nearby star-forming galaxies (e.g. Adamo, Östlin & Zackrisson 2011; Messa et al. 2018) and reproduced in a theoretical framework in which stellar clusters arise naturally at the highest density end of the hierarchy of the interstellar medium (Kruijssen 2012; Li et al. 2017). In particular, Γ increases to values higher than 50 per cent when the SFRSD is $\text{Log}_{10}(\Sigma_{\text{SFR}}) > 1$, eventually flattening to > 90 per cent if $\text{Log}_{10}(\Sigma_{\text{SFR}}) > 2$, a regime in which the

density of the gas is so high that nearly only bound structures form (Adamo & Bastian 2018). The $\Gamma - \Sigma_{\text{SFR}}$ relation, which reflects the more fundamental $\Gamma - \Sigma_{\text{GAS}}$ relation, shows how the galactic and/or the star-forming complex environment affects the clustering properties of the star formation process.

The system D1T1 presented in this work is part of a possible larger structure counting a dozen of individual sources presumably distributed at $z \sim 6$, distributed on a relatively small volume (several tens kpc), and that will be better defined with the ongoing deep MUSE observations (Vanzella et al., in preparation). If we focus on the system D1T1 and interpret it as a star-forming complex with a size of about 800 pc across (fully including T1 and D1, Fig. 2), adopting the best SFRs estimates reported in Table 1, then the global $\text{Log}_{10}(\Sigma_{\text{SFR}})_{\text{D1T1}} \sim 1.3$ would imply a relatively large cluster formation efficiency, $\Gamma > 40$ per cent (if the relation observed in the local Universe is valid also at high redshift; Messa et al. 2018). Such a relatively high value is also expected at high redshift (Kruijssen 2012). Moreover, the possible ongoing interaction (or merging) between the systems T1 and D1, connected by an elongated structure which looks like a stellar stream, suggests the presence of YMCs, as it has been observed locally in merging galaxies showing also a systematically higher truncation mass (or upper mass limit) in the initial cluster mass function (e.g. as in the *Antennae* galaxies; Portegies Zwart et al. 2010).

Therefore, putting together the two arguments (high Γ and a possible high truncation mass of the initial star cluster mass function in merging systems), it would not be surprising that several compact and dense knots, including the core of D1, T1, and UT1, have been identified within the complex we are investigating and might be the manifestation of a high cluster formation efficiency (see also UT2 and UT3 knots indicated in Fig. 2). The identification of a single gravitationally bound massive star cluster is the next step

and the nucleated emission hosted by D1 and discussed in this work might support such a possibility, though only future facilities (like *JWST* and E-ELT) can fully address this issue. However, it is worth noting that the observed stellar mass of D1 ($2 \times 10^7 M_\odot$) is also consistent with the presence of a single massive cluster (in the present case with a stellar mass of $\sim 10^6 M_\odot$). Indeed, following equation (4) and discussion in Elmegreen & Elmegreen (2017) (see also, Howard, Pudritz & William E. 2018), the total expected mass of a star-forming region hosting a single massive cluster with $M = 10^6 M_\odot$ is $M_{\text{star}} \simeq 2 \times 10^7 M_\odot$, a mass that is fully consistent with what inferred for D1. This mass is also compatible for the values expected in some scenarios for GC formation, in which such systems host multiple stellar populations (D’Ercole et al. 2008; Calura et al. 2015; Vanzella et al. 2017b; Calura et al., in preparation).

Another question we might ask is: what is the evolutionary stage of the innermost dense forming region? The inferred Σ_{SFR} is extremely high ($\text{Log}_{10}(\Sigma_{\text{SFR}}) > 2.5$ or $\simeq 3$) and might suggest it is experiencing the first phases of star formation in a star cluster-like object.

4.1.1 Comparison with local YMCs: dense star formation

The inferred Σ_{SFR} in the core is consistent with what is expected in the densest star-forming YMCs observed locally. A simple estimate of the Σ_{SFR} of YMCs hosted in local galaxies (within 10 Mpc distance) can be derived from the recent release of the catalogue of young star clusters observed in the LEGUS survey (PI: Calzetti; Calzetti et al. 2015), from which effective radii, stellar masses, and ages have been derived for dozens of bound stellar systems and in the mass range of $\sim (0.01-1) \times 10^6 M_\odot$ (e.g. Adamo et al. 2017; Ryon et al. 2017). As an example, the SSC hosted by the ultracompact dwarf galaxy NGC1705 shows an effective radius of $R_e = 4$ pc,⁸ a stellar mass of $7.15 \times 10^5 M_\odot$, and an age of 15 Myr. The Σ_{SFR} can be calculated as follows: $(0.5 \times M/\Delta t)/(\pi R_{\text{hm}}^2)$, where M is the stellar mass of the cluster, the factor 0.5 accounts for the half-mass radius we used in the calculation, R_{hm} [and $R_{\text{hm}} = (4/3)R_e$; Portegies Zwart et al. 2010] and Δt is the age of the cluster. The Σ_{SFR} calculated for the SSC of NGC1705 is $\text{Log}_{10}(\Sigma_{\text{SFR}}) > 2.4$. Relatively massive young star clusters have been identified in the interacting *Antennae* galaxies (NGC 4038/4039), with stellar masses of a few $10^6 M_\odot$ and effective radii in the range $R_e \simeq 1-8$ pc. In particular, the cluster W99-2 reported by Mengel et al. (2008) (see also Portegies Zwart et al. 2010) with $R_e = 8$ pc, age 6.6 Myr, and stellar mass $2.63 \times 10^6 M_\odot$ is among the most massive and largest clusters studied in that merging galaxy, having a $\text{Log}_{10}(\Sigma_{\text{SFR}}) > 2.75$ (calculated as discussed above). Clearly the above Σ_{SFR} are very conservative lower limits since the bulk of the star formation plausibly occurred on a shorter time-scale. In the case of the SSC of NGC 1705, if we assume a duration of the burst lower than 5 Myr then a much larger value is obtained, $\text{Log}_{10}(\Sigma_{\text{SFR}}) \sim 2.9$, not dissimilar to what we inferred for the D1(core), and close to the upper edge of the SK-law, approaching the maximum Eddington-limited star formation rate per unit area discussed by Crocker et al. (2018). Similarly, also W99-2 SSC might have experienced a Σ_{SFR} higher than $1000 M_\odot \text{ yr}^{-1} \text{ kpc}^{-2}$ if the star formation history was confined within the first 3 Myr (i.e. within the 50 per cent of its age).

⁸From the LEGUS catalogue the concentration index for this cluster, CI, is 1.87, and corresponds to a 4 pixel effective radius, that at the distance of NGC1705 of 5.1 Mpc translates to 4 pc, see fig. 4 of Adamo et al. (2017).

The detection of massive ($\gtrsim 10^6 M_\odot$) and young (< 10 Myr) star cluster populations in *late*-stage mergers such as the *Antennae* galaxies (including also Arp 220 and the Mice galaxies NGC 4676 A/B), has been statistically extended recently with a sample of 22 local LIRGs showing ongoing merging (Linden et al. 2017). In such big merger events, hydrodynamic simulations show that the ISM condition can produce clusters in the mass range $10^{5.5} < M < 10^{7.5} M_\odot$ (Maji et al. 2017). Presumably, in the present case (though at a lower mass regime with respect to LIRGs), the interacting D1T1 *early*-stage system might contain similar massive star clusters possibly forming during a proto-galaxy phase (e.g. Peebles & Dicke 1968). The initial star cluster mass function (and cluster formation efficiency) in such early conditions (at $z = 6$) is at the moment observationally unknown, however it is possible that interacting systems, such as D1T1, might have experienced the formation of high-mass star clusters as observed in local mergers. Frequent mergers in high-redshift proto-galaxies provide a fertile environment to produce populations of bound clusters by pushing large gas masses ($10^{5-6} M_\odot$) collectively to high density, at which point it can (rapidly collapse and) turn into stars before stellar feedback can disrupt the clouds (e.g. Kim et al. 2018).

4.1.2 A globular cluster precursor ?

So far, the search for local analogues of GC precursors has led to inconclusive results (Portegies Zwart et al. 2010; Bastian et al. 2013), as no convincing evidence of multiple stellar populations has been found in local YMCs (Bastian & Lardo 2018). The search of forming GCs at high redshift is even more challenging, for several reasons. First, as a necessary condition, YMCs have to be identified and second, the GCP has to be associated in some way. The first point is now addressable thanks to a widely improved set of strong lensing models coupled with deep integral field spectroscopy (e.g. VLT/MUSE) and *HST* multiband observations (like the HFFs), such as the case of D1(core) presented in this work. In addition, the expected occurrence of forming GCs at $z > 3$ is high (Renzini 2017; Vanzella et al. 2017b; Bouwens et al. 2018), and their detectability is feasible nowadays. The second point is strongly related to current globular cluster formation theories, with key parameters represented by the original masses and sizes of proto-GCs (see recently, Terlevich et al. 2018).

As discussed in the previous sections, it is very plausible that the D1(core) is dominated by (or represents itself) a young massive star cluster detected in the first few million years after the onset of a burst of star formation. D1 extends ~ 440 pc and is part of a larger star-forming complex (that includes D1 and T1 of ~ 800 pc across) showing possible interacting components as outlined by the stellar stream connecting D1, T1, and UT1. It is worth discussing if D1(core) (the possible SSC with the highest S/N detection we have) and its environment can present the expected condition of a forming GC. Only those clusters that survive the disruption processes and are still dense and gravitationally bound can likely become the globular clusters we observe today. Clearly any inference on what D1T1 would appear today is totally model dependent.

First, we notice that the apparent central position of any nucleated star cluster in D1 might be compatible with the scheme suggested by Goodman & Bekki (2018) for the formation of ultracompact dwarf galaxies (UCD), in which one possible formation path is the tidal thrashing of a nucleated elliptical dwarf galaxy, after massive star clusters (originated in off-centre GCM) migrated towards the centre of the potential well according on a time-scale dictated by

dynamical friction (Binney & Tremaine 1987; Goodman & Bekki 2018). With a stellar mass of $\sim 2 \times 10^7 M_{\odot}$, an effective radius of ~ 40 pc and age younger than 100 Myr, D1 might be in the formation phase of an ultracompact dwarf, in particular the M4 and M5 models of Goodman & Bekki (2018) in terms of mass and half-mass radius (assuming the half-light radius in the UV is not dissimilar than the optical one). Interestingly, the presence of the companion T1 (at ~ 500 pc distance) and a stellar bridge connecting the two objects (see Fig. 2), may also suggest a possible ongoing interaction, mirroring the tidal thrashing mentioned above.

Secondly, UCDs share many properties with massive globular clusters, such that dwarf-globular transition objects might blur the distinction between compact stellar clusters and dwarfs (e.g. Forbes et al. 2008; Goodman & Bekki 2018) and this is the reason why – in scenarios in which GCs form in dwarfs – high-redshift galaxies at the faint end of the UV luminosity function will inevitably match the same observational conditions as GC precursors. It is not the scope of this work to establish the link between the presence of YMCs in the system D1T1 and the potential nature of proto-GCs, and perhaps no strong evidence has been found to date, at any redshift. However, it is fair to say that GCPs have in good probability already been detected, but in most cases not recognized, yet. It is worth noting that some ancient local dwarf galaxies host possible GCs in their cores, suggesting that in some cases, the star cluster and its environment (or hosting dwarf) survived for the entire cosmic time (e.g. Cusano et al. 2016; Zaritsky, Crnojević & Sand 2016).

The system reported in this work, i.e. the superdense and compact star-forming region of $\lesssim 10^6 M_{\odot}$ located in a forming dwarf (D1) undergoing an interaction with a close companion (T1) surrounded by an extended Ly α emitting region represents one of the most promising cradle hosting a GCP (e.g. Elmegreen et al. 2012; Trenti, Padoan & Jimenez 2015; Ricotti et al. 2016; Renzini 2017; Goodman & Bekki 2018; Kim et al. 2018; Terlevich et al. 2018; Zick et al. 2018). The reader is allowed to accommodate our system into their preferred GC formation scenario. In any such scenario, the unknown mass of the present-day by-product of D1 (assuming it has survived down to $z = 0$ as a gravitationally bound GC) will be determined by whether the entire D1 object or only its most nucleated region [D1(core)] might be regarded as GCP, especially in the light of the mass-budget argument (see e.g. Renzini et al. 2015; Vanzella et al. 2017b).

4.2 The Ly α nebulae surrounding the star-forming complex: what is its origin?

Local YMCs usually host a large population of very massive stars (e.g. R136 in the 30 Doradus; Crowther et al. 2016), therefore ionizing radiation and feedback from young clusters may have important effects also at large distances (e.g. hundreds of pc and up to kpc scale; Annibali et al. 2015; Smith et al. 2016). A detailed analysis of the Ly α emission and spatial variation along the arc will be better characterized with the AO-assisted MUSE deep lensed field. However, the strong Ly α emission discussed in Section 2.3.1 (with equivalent width larger than 120 Å rest frame) suggests an intense ionizing radiation field consistent with the emission of young stellar populations and a remarkably low opacity at the – resonant – Ly α transition, allowing for a large escape fraction of Ly α photons [EW(Ly α) > 100 Å]. Both the presence of dense H I gas and dust would concur to significantly depress the line, whose prominence, instead, implies that some feedback is in place, either in the form of outflowing gas that moves Ly α photons away from the resonance frequency (and therefore decreasing the amount of scattering and

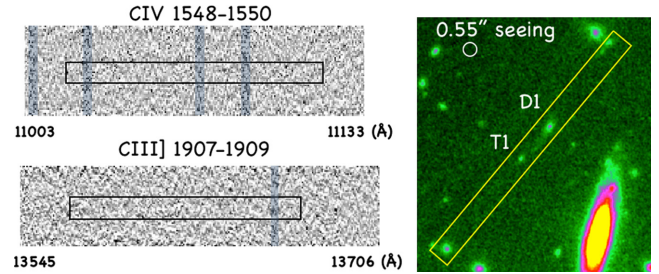


Figure 11. Two hours X-Shooter observations of the system D1T1. On the right-hand side the slit orientation is shown superimposed to the WFC3/F105W band. The diameter of the white circle corresponds to the average seeing during observations, 0.55 arcsec. A nodding in two positions of 1.2 arcsec has been performed. In the left-hand panels, the zoomed spectral regions around CIV and C III] lines are shown. The black boxes mark the positions and the wavelength intervals within ± 1000 km s $^{-1}$ from the Ly α redshift ($z = 6.143$). Vertical grey stripes marks the position of the most prominent sky emission lines. At the current depth no lines have been detected (see the text for more details).

the probability to encounter dust grains) or as already carved ionized channels that allow Ly α photons to freely escape and scatter in the circumgalactic medium up to kpc distances. Such a kpc-scale Ly α nebula might also be produced by ionizing photons that escape from the D1T1 complex along the same (or similar) transparent routes and induce Ly α fluorescence (e.g. as it has been observed in a much brighter regime at $z = 4$; Vanzella et al. 2018). Only JWST will allow us to observe the same arc at the Balmer H α wavelength, eventually probing any fluorescing nature (NIRSPEC/IFU observing at 4.7 μ m). This will address the possible contribution of high-redshift YMCs to the ionizing radiation field far (by several kpc) from regions where the star formation occurs, eventually quantifying the local escaping ionizing radiation and the possible role of GCPs to the ionization of the intergalactic medium.

4.3 The intermediate mass black hole possibility

The fact that D1(core) is spatially not resolved leaves room for the possible presence of a faint AGN. In such conditions, a hosting galaxy with a stellar mass of a few $10^7 M_{\odot}$ would imply an intermediate mass black hole (IMBH) with mass of the order of $\simeq 10^4 M_{\odot}$ (Kormendy & Ho 2013). Assuming the underlying spectrum for the IMBH is the same as observed in brighter AGNs, the presence of high-ionization lines and line ratios could be used to investigate the nature of the ionizing source (e.g. Feltre, Charlot & Gutkin 2016; Gutkin, Charlot & Bruzual 2016). To this aim, two hours VLT/X-Shooter observations (ID 098.A-0665B, PI: E. Vanzella) have been spent during 2017 September with optimal seeing conditions, 0.53 and 0.57 arcsec for the two OBs. The slit orientation is shown in Fig. 11 in which a dithering pattern of 1.2 arcsec has been implemented (to avoid superposition among D1 and T1). Data reduction has been performed adopting the same procedures described in Vanzella et al. (2017c) (see also, Vanzella et al. 2016a). These exploratory observations provide no detections of CIV λ 1548, 1550 and C III] λ 1908 lines down to $\sim 3 \times 10^{-18}$ erg s $^{-1}$ cm $^{-2}$ at the 1σ level, neither for T1 nor D1, assuming such lines arise at $z = 6.143 \pm 0.025$, i.e. ± 1000 km s $^{-1}$ from Ly α emission (Fig. 11). While deeper observations are certainly needed to better explore such transitions, including nebular high-ionization lines of stellar origin (as narrow as a few km s $^{-1}$ velocity dispersion; Vanzella et al. 2017c), the shallow limits currently available imply

$\text{Ly}\alpha/\text{C IV} > 8(22)$ for the D1T1 system, adopting the $\text{Ly}\alpha$ flux measured in the *local(global)* aperture, as discussed in Section 2.3.1 (flux($\text{Ly}\alpha$) = $2.5(6.7) \times 10^{-17}$ erg s $^{-1}$ cm $^{-2}$), possibly excluding any evident AGNs (e.g. Alexandroff et al. 2013). Similarly, no $\text{N V } \lambda 1240$ has been detected in the MUSE data cube, providing a $\text{Ly}\alpha/\text{N V } \lambda 1240 > 18$ at the 1σ limit. This is a very conservative lower limit if we consider that the $\text{Ly}\alpha$ flux is also a lower limit (see Section 2.3.1). This limit is higher than the typical values reported for AGNs at moderate ($z \sim 2-3$) and high ($z > 5$) redshifts (see discussion in Castellano et al. 2018). While the possible presence of an IMBH would be extremely interesting, being such objects never been observed (especially at high redshift) and representing a current challenge for the theoretical models of BH and structure formation (e.g. Reines & Comastri 2016; Pacucci et al. 2018), the current data are consistent with the star cluster interpretation.

5 SUMMARY AND CONCLUSIONS

We studied an ideal case in which a dwarf galaxy hosting a nucleated ultraviolet emission is significantly stretched due to gravitational lensing. Firm constraints on a star-forming region of unprecedented small size at $z = 6.1$ have been achieved. The present constraints pave the way towards a possible future unambiguous detection of a forming SSC in the first Gyr of the universe. In particular:

(i) A superdense and compact star-forming region, D1(core), with $R_e < 13$ pc in a dwarf galaxy (D1, extending up to ~ 440 pc) is confirmed at $z = 6.143$, which is, in turn, part of a larger and interacting star-forming complex that includes D1 and T1 (extending to ~ 800 pc across). D1 and T1 are spatially resolved and connected by a stellar stream also containing an ultrafaint star-forming knot (indicated as UT1, Fig. 2). The D1(core) shows a circular symmetric shape fully consistent with the *HST* PSF despite the large gravitational stretch well depicted by the giant tangential $\text{Ly}\alpha$ arc.

(ii) Extensive GALFIT modelling and MC simulations clearly demonstrate the compactness of D1(core) that also accounts for the (25–30) percent of the ultraviolet light of the entire dwarf galaxy D1, implying a very large SFRSD occurred in such a compact region. After including realistic uncertainties on the magnification, morphology and the SFR, the SFRSD is quite large, $\Sigma_{\text{SFR}} > 300 M_{\odot} \text{ yr}^{-1} \text{ kpc}^{-2}$ in the conservative case, or $\Sigma_{\text{SFR}} > 800 M_{\odot} \text{ yr}^{-1} \text{ kpc}^{-2}$ as a best estimate. The comparison of the same expected quantity derived for local YMCs during their formation phase ($\Sigma_{\text{SFR}} \simeq 1000 M_{\odot} \text{ yr}^{-1} \text{ kpc}^{-2}$) suggests the D1(core) is fully compatible with being a fresh SSC with a stellar mass of $\lesssim 10^6 M_{\odot}$ and observed just a few Myr after the onset of the star formation. The stellar mass of the hosting galaxy D1 of $2 \times 10^7 M_{\odot}$ is also consistent with the presence of such a massive cluster. Accordingly to several scenarios, such a system is an ideal candidate globular cluster precursor.

The ultraviolet appearance of D1 and its core also match those of the ultracompact dwarf galaxy NGC 1705 simulated at $z = 6.143$ and strongly lensed via the SKYLENS tool through our currently best lens model for the HFF cluster MACS J0416. NGC 1705 contains a well-known young SSC. Both the host galaxy, NGC 1705, and its SSC, show very similar luminosities and masses as estimated for D1 and D1(core), respectively (see Table 1).

The prominent $\text{Ly}\alpha$ emission of equivalent width larger than 120 \AA rest frame surrounding the system D1T1, extending up to 5 kpc (much larger than the detected stellar continuum of the D1T1 stellar complex, $\lesssim 1$ kpc) and the very blue ultraviolet spectral slope ($\beta = -2.50 \pm 0.10$) suggest the underlying stellar populations are

very young ($< 10-100$ Myr) and with very little dust attenuation. $\text{Ly}\alpha$ photons are very sensitive to dust absorption, especially in presence of very dense H I gas (e.g. Verhamme, Schaerer & Maselli 2006), as the high Σ_{SFR} seems to imply. An enhanced $\text{Ly}\alpha$ visibility can be related to ongoing feedback through outflows and/or carved ionized channels. However, the real nature of the $\text{Ly}\alpha$ nebula is still unknown: it can be the result of pure $\text{Ly}\alpha$ scattering or fluorescence induced by escaping ionizing radiation, or both. Fluorescence is also connected to the ionization power of such tiny sources in the framework of cosmic reionization, certainly worth investigating in the future.

5.1 Caveats and future prospects

While the investigation of parsec-scale ($\lesssim 20$ pc) star-forming regions at $z = 2-6$ represent the state-of-the-art analysis, joining deep *HST* imaging, strong lensing and integral field spectroscopy, there are still caveats that limit the current studies. We list in the following the significant improvements on the specific system studied here (D1T1) that can be achieved with future facilities. The same considerations are equally applicable to the most general framework of star cluster searches at cosmological distances and their influence to the surrounding medium (feedback, ionization).

(i) *Spatial resolution*: It is unknown what is the distribution of the size (R_e) of the most compact SF regions currently identified at high redshift, like the core of D1. A significant leap will be performed with future instrumentation which will provide spatial resolution down to 20 mas (e.g. VLT/MAVIS in the optical, $\lambda < 1 \mu\text{m}$) or 10 mas (E-ELT/MAORY + MICADO in the near-infrared with MCAO narrow field mode and much larger collecting area). Such PSFs, in the specific case (of D1) and along the maximum magnification, will probe light profiles down to 4–8 pc resolution, eventually resolving the small, possibly gravitationally bound, star clusters. Ground-based high spatial resolution imaging will be limited to the blue/ultraviolet at $z > 5$ (the *K*-band probing $\lambda < 3800 \text{ \AA}$ rest frame). In the case of D1T1, only *JWST* will provide morphological information at optical rest-frame wavelengths ($\simeq 6000-8000 \text{ \AA}$), in which the size and the stellar mass can be properly estimated, as well as the stellar mass surface density.

(ii) *Spectral coverage*: While at $z \sim 3$ the accessible spectral range from ground-based facilities still covers the rest-frame optical (and marginally the $\text{H}\alpha$ line, though limited to $z < 2.5$), at $z > 4$ the rest-frame optical (e.g. the Balmer lines $\text{H}\beta$, $\text{H}\alpha$, and metal lines) is redshifted into the $> 2.4 \mu\text{m}$ range. In the case of D1T1 the $\text{H}\alpha$ lies at $4.66 \mu\text{m}$, observable only with *JWST*. The $\text{H}\alpha$ line is the best SFR indicator, and by means of the NIR-SPEC/IFU (integral filed unit onboard *JWST*) the nature of the $\text{Ly}\alpha$ nebula (scattering versus fluorescence) can be investigated. The access to the optical rest frame, both with imaging and spectroscopy, will also definitely improve the estimate of the physical properties of such potential GCPs (e.g. stellar mass, age, SFR, dust content, and nebular attenuation via the Balmer lines decrement).

(iii) *Statistics*: Despite the power of strong lensing and the positive prospects in the improvement of future lensing models, large distortion of the images (e.g. large values of $\mu_{\text{tang}}/\mu_{\text{rad}}$) might hide features potentially missed in a single object. Indeed, in the case of D1T1, whatever small source lying along the radial direction within ~ 130 pc from D1 would be spatially unresolved or merged into a single object, i.e. it would be PSF dominated. In such a case the

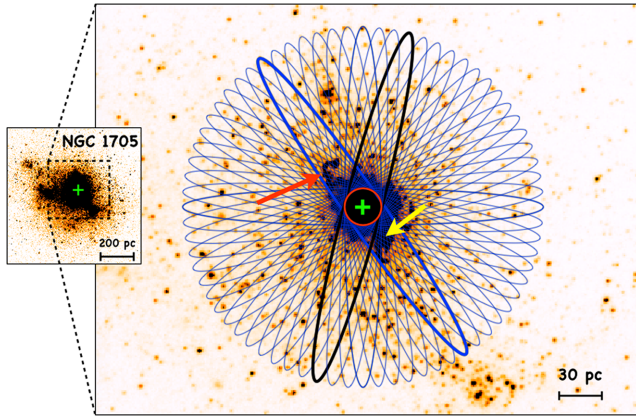


Figure 12. A calculation of light contamination from star-forming complexes surrounding the SSC due to lensing stretch ($\mu_{\text{tang}}/\mu_{\text{rad}} \simeq 10$). The blue ellipses have semiminor and semimajor axes of 13 and 130 pc, corresponding to the limits we calculated along tangential and radial directions for the $z = 6.14$ arc, respectively. The median flux is computed from 36 ellipses placed with different PAs (with step of 5 deg from each other) and all centred on the SSC (marked with a green cross), and subsequently compared to the flux derived from the circular aperture of 13 pc radius (red circle), centred at the same position. The maximum/minimum ratio [counts(ellipse)/counts(circle)] happens at the blue/black thick ellipse, corresponding to overestimated fluxes by factors 1.52 and 1.30, respectively (see the text for more details). The maximum ratio is given by the inclusion in the ellipse of two structures: a star-forming complex (indicated with a red arrow) and a star cluster (indicated with a yellow arrow, dubbed star cluster ‘1’ by Annibali et al. 2009) both at $\simeq 23$ pc away from the main SSC. An image of NGC 1705 is shown in the leftmost inset, in which the dashed square outline the zoomed region shown in the main panel.

inferred luminosity of the star cluster would be overestimated. In particular, as a test-case, we inferred the amount of light contamination for NGC 1705 by calculating the flux within ellipses of 13 pc \times 130 pc (of semiminor and semimajor axis) centred on the SSC and placed over 36 PAs (with a step of 5 deg), and compared to the flux measured on a circular aperture of 13 pc radius centred on the same SSC (see Fig. 12). On average the light measured on the elliptical apertures is overestimated by a median factor $1.36^{+0.16}_{-0.06}$ (68 per cent interval), corresponding to ~ 0.34 mag. Therefore, assuming the analogy among D1 and NGC 1705, this test would imply the star cluster hosted in the core of D1 would be $\simeq 0.3$ – 0.4 mag fainter than what is measured (corresponding to $M_{\text{UV}} \simeq -15.2$). An even worse case would correspond to multiple star clusters aligned along the radial direction and not spatially resolved. Assuming a pair of (equal-mass) not spatially resolved SSCs, the true luminosity of each one would be overestimated by a factor 2 (or 0.75 mag). As mentioned above, future observations with high spatial resolution facilities (like ELT and VLT/MAVIS) will dramatically improve the situation. This orientation effect, however, can be washed out after averaging over several D1T1-like sources and/or candidate star clusters/star-forming complexes. From the initial analysis presented in this work, the compactness of several individual knots in the $z = 6.14$ system, spanning the interval 13 pc $< R_e < 50$ pc, already suggest that D1(core), T1, UT1 (including T3 and T4, see Section 2.1) are intrinsically small objects, unless all of them are elongated along the same radial direction. The increasing effort with dedicated *HST* programs focusing on galaxy clusters (like CLASH, HFFs, RELICS, e.g. Postman et al. 2012; Lotz et al. 2017; Coe et al. 2018) will timely

produce the statistical significant sample for the current facilities, like ALMA, and the forthcoming ELT and *JWST*. VLT/MUSE will continue to play a crucial role in the spectroscopic identification of hundreds of multiple faint images in the redshift range $3 < z < 6.5$, useful for tuning the lens models and extending the discovery space of tiny star clusters, and eventually the population of GCPs.

Before the advent of *JWST* and E-ELT, further progress can be achieved by performing deep spectroscopy in the near-infrared wavelengths and look for nebular high-ionization lines. Indeed, such candidate SSC(s) may contain significant amount of massive and hot stars ($T_{\text{eff}} > 50$ kK), sufficiently hot to emit photons more energetic than 4 Ryd and produce emission lines up to the He II $\lambda 1640$ (as observed in the case of the YMC R136 in 30 Doradus; Crowther et al. 2016, and more recently Lennon et al. 2018).

ACKNOWLEDGEMENTS

We thank the referee for providing constructive comments. We thank M. Tosi, L. Hunt, F. Annibali, A. Adamo, and F. Cusano for the very useful discussions about local dwarf star-forming galaxies and young massive star clusters, and P. Ciliegi, M. Bellazzini, and E. Diolaiti for useful discussions about the MAORY specifications. EV thanks A. Ferrara, N. Gnedin, R. Ellis, H. Katz, D. Sobral, and R. Bouwens for stimulating discussions during the Munich Institute for Astro- and Particle Physics (MIAPP) workshop about the nature of the tiny sources presented in this work, and A. Renzini, N. Bastian, and E. Dalessandro for sharing their thoughts about the GCPs. FC and AM acknowledge funding from the INAF PRIN-SKA 2017 program 1.05.01.88.04. MM acknowledges support from the Italian Ministry of Foreign Affairs and International Cooperation, Directorate General for Country Promotion. Based on observations collected at the European Southern Observatory for Astronomical research in the Southern hemisphere under ESO programme 098.A-0665(B).

REFERENCES

- Adamo A., Östlin G., Zackrisson E., 2011, *MNRAS*, 417, 1904
 Adamo A. et al., 2017, *ApJ*, 841, 131
 Adamo A., Bastian N., 2018, in Steven S., ed., *Astrophysics and Space Science Library*, Vol. 424, *The Birth of Star Clusters*. Springer-Verlag, Berlin, p. 91
 Alavi A. et al., 2016, *ApJ*, 832, 56
 Alexandroff R. et al., 2013, *MNRAS*, 435, 3306
 Anderson J., 2016, WFC3/ISR 2016-12. STScI, Baltimore
 Annibali F., Tosi M., Monelli M., Sirianni M., Montegriffo P., Aloisi A., Greggio L., 2009, *AJ*, 138, 169
 Annibali F., Tosi M., Pasquali A., Aloisi A., Mignoli M., Romano D., 2015, *AJ*, 150, 143
 Atek H., Richard J., Kneib J.-P., Schaerer D., 2018, *MNRAS*, 479, 5184
 Bacon R. et al., 2010, Proc. SPIE Conf. Ser. Vol. 7735, *The MUSE Second-Generation VLT Instrument*. SPIE, Bellingham, p. 773508
 Bacon R. et al., 2015, *A&A*, 575, A75
 Bastian N., 2008, *MNRAS*, 390, 759
 Bastian N., Lardo C., 2018, *ARA&A*, 56, 83
 Bastian N., Cabrera-Ziri I., Davies B., Larsen S. S., 2013, *MNRAS*, 436, 2852
 Behrens C., Dijkstra M., Niemeyer J. C., 2014, *A&A*, 563, A77
 Bigiel F., Leroy A., Walter F., Blitz L., Brinks E., de Blok W. J. G., Madore B., 2010, *AJ*, 140, 1194

- Binney J., Tremaine S., 1987, *Galactic Dynamics*. Princeton Univ. Press, Princeton, NJ, p. 747
- Bouwens R. J. et al., 2016a, *ApJ*, 830, 67
- Bouwens R. J., Smit R., Labbé I., Franx M., Caruana J., Oesch P., Stefanon M., Rasappu N., 2016b, *ApJ*, 831, 176
- Bouwens R. J., van Dokkum P. G., Illingworth G. D., Oesch P. A., Maseda M., Ribeiro B., Stefanon M., Lam D., 2018, *ApJ*, preprint (arXiv:1711.02090)
- Boylan-Kolchin M., 2018, *MNRAS*, 479, 332
- Bruzual G., Charlot S., 2003, *MNRAS*, 344, 1000
- Calura F., Few C. G., Romano D., D’Ercole A., 2015, *ApJ*, 814, L14
- Calzetti D., Armus L., Bohlin R. C., Kinney A. L., Koornneef J., Storchi-Bergmann T., 2000, *ApJ*, 533, 682
- Calzetti D. et al., 2015, *AJ*, 149, 51
- Caminha G. B. et al., 2016, *A&A*, 595, A100
- Caminha G. B. et al., 2017a, *A&A*, 600, A90
- Caminha G. B. et al., 2017b, *A&A*, 607, A93
- Castellano M. et al., 2016, *A&A*, 590, A31
- Castellano M. et al., 2018, *ApJ*, 863, L3
- Cava A., Schaerer D., Richard J., Pérez-González P. G., Dessauges-Zavadsky M., Mayer L., Tamburello V., 2018, *Nat. Astron.*, 2, 76
- Coe D. et al., 2018, American Astronomical Society, AAS Meeting #231, 454.10
- Crocker R. M., Krumholz M. R., Thompson T. A., Clutterbuck J., 2018, *MNRAS*, 478, 81
- Crowther P. A. et al., 2016, *MNRAS*, 458, 624
- Cusano F. et al., 2016, *ApJ*, 829, 26
- Dayal P., Ferrara A., 2018, *Phys. Rep.*, 780, 1
- De Barros S. et al., 2017, *A&A*, 608, A123
- Dessauges-Zavadsky M., Schaerer D., Cava A., Mayer L., Tamburello V., 2017, *ApJ*, 836, L22
- Dessauges-Zavadsky M., Adamo A., 2018, *MNRAS*, 479, L118
- D’Ercole A., Vesperini E., D’Antona F., McMillan S. L. W., Recchi S., 2008, *MNRAS*, 391, 825
- Elmegreen B. G., Malhotra S., Rhoads J., 2012, *ApJ*, 757, 9
- Elmegreen B. G., Elmegreen D. M., Sánchez Almeida J., Muñoz-Tuñón C., Dewberry J., Putko J., Teich Y., Popinchalk M., 2013, *ApJ*, 774, 86
- Elmegreen D. M., Elmegreen B. G., 2017, *ApJ*, 851, L44
- Feltre A., Charlot S., Gutkin J., 2016, *MNRAS*, 456, 3354
- Finkelstein S. L. et al., 2015, *ApJ*, 810, 71
- Forbes D. A., Lasky P., Graham A. W., Spitler L., 2008, *MNRAS*, 389, 1924
- Förster Schreiber N. M. et al., 2011, *ApJ*, 739, 45
- Gallego S. G. et al., 2018, *MNRAS*, 475, 3854
- Genzel R. et al., 2011, *ApJ*, 733, 101
- Goodman M., Bekki K., 2018, *MNRAS*, 478, 3564
- Grillo C. et al., 2015, *ApJ*, 800, 38
- Guo Y., Giavalisco M., Ferguson H. C., Cassata P., Koekemoer A. M., 2012, *ApJ*, 757, 120
- Gutkin J., Charlot S., Bruzual G., 2016, *MNRAS*, 462, 1757
- Hayes M., Schaerer D., Östlin G., Mas-Hesse J. M., Atek H., Kunth D., 2011, *ApJ*, 730, 8
- Howard C. S., Pudritz R. E., William E. Harris., 2018, *Nat. Astron.*, 2, 725
- Johnson T. L. et al., 2017, *ApJ*, 843, 78
- Karman W. et al., 2017, *A&A*, 599, A28
- Katz H., Ricotti M., 2013, *MNRAS*, 432, 3250
- Kawamata R., Ishigaki M., Shimasaku K., Oguri M., Ouchi M., 2015, *ApJ*, 804, 103
- Kennicutt R. C., Jr, 1998a, *ARA&A*, 36, 189
- Kennicutt R. C., Jr, 1998b, *ApJ*, 498, 541
- Kim J.-h. et al., 2018, *MNRAS*, 474, 4232
- Kormendy J., Ho L. C., 2013, *ARA&A*, 51, 511
- Krujssens J. M. D., 2012, *MNRAS*, 426, 3008
- Laursen P., Sommer-Larsen J., Razoumov A. O., 2011, *ApJ*, 728, 52
- Leclercq F. et al., 2017, *A&A*, 608, A8
- Lennon D. J. et al., 2018, *A&A*, 619, A78
- Li H., Gnedin O. Y., Gnedin N. Y., Meng X., Semenov V. A., Kravtsov A. V., 2017, *ApJ*, 834, 69
- Linden S. T. et al., 2017, *ApJ*, 843, 91
- Livermore R. C. et al., 2015, *MNRAS*, 450, 1812
- Lotz J. M. et al., 2017, *ApJ*, 837, 97
- Mahler G. et al., 2018, *MNRAS*, 473, 663
- Maji M., Zhu Q., Li Y., Charlton J., Hernquist L., Knebe A., 2017, *ApJ*, 844, 108
- Mas-Ribas L., Hennawi J. F., Dijkstra M., Davies F. B., Stern J., Rix H.-W., 2017, *ApJ*, 846, 11
- Meneghetti M. et al., 2008, *A&A*, 482, 403
- Meneghetti M., Rasia E., Merten J., Bellagamba F., Ettori S., Mazzotta P., Dolag K., Marri S., 2010, *A&A*, 514, A93
- Meneghetti M. et al., 2017, *MNRAS*, 472, 3177
- Mengel S., Lehnert M. D., Thatte N. A., Vacca W. D., Whitmore B., Chandar R., 2008, *A&A*, 489, 1091
- Merlin E. et al., 2016, *A&A*, 590, A30
- Messa M. et al., 2018, *MNRAS*, 473, 996
- Pacucci F., Loeb A., Mezcua M., Martín-Navarro I., 2018, *ApJ*, 864, L6
- Peebles P. J. E., Dicke R. H., 1968, *ApJ*, 154, 891
- Peng C. Y., Ho L. C., Impey C. D., Rix H.-W., 2002, *AJ*, 124, 266
- Peng C. Y., Ho L. C., Impey C. D., Rix H.-W., 2010, *AJ*, 139, 2097
- Plazas A. A., Meneghetti M., Maturi M., Rhodes J., 2019, *MNRAS*, 482, 2823
- Portegies Zwart S. F., McMillan S. L. W., Gieles M., 2010, *ARA&A*, 48, 431
- Postman M. et al., 2012, *ApJ*, 199, 25
- Reines A. E., Comastri A., 2016, *PASA*, 33, e054
- Renaud F., 2018, *New Astron. Rev.*, 81, 1
- Renzini A. et al., 2015, *MNRAS*, 454, 4197
- Renzini A., 2017, *MNRAS*, 469, L63
- Ricotti M., 2002, *MNRAS*, 336, L33
- Ricotti M., Parry O. H., Gnedin N. Y., 2016, *ApJ*, 831, 204
- Rifatto A., Longo G., Capaccioli M., 1995, *A&AS*, 114, 527
- Rigby J. R. et al., 2017, *ApJ*, 843, 79
- Robertson B. E., Ellis R. S., Furlanetto S. R., Dunlop J. S., 2015, *ApJ*, 802, L19
- Ryon J. E. et al., 2017, *ApJ*, 841, 92
- Salpeter E. E., 1955, *ApJ*, 121, 161
- Schaerer D., 2002, *A&A*, 382, 28
- Schaerer D., Charbonnel C., 2011, *MNRAS*, 413, 2297
- Shi Y. et al., 2018, *ApJ*, 853, 149
- Smith L. J., Crowther P. A., Calzetti D., Sidoli F., 2016, *ApJ*, 823, 38
- Stark D. P. et al., 2014, *MNRAS*, 445, 3200
- Stark D. P. et al., 2015a, *MNRAS*, 450, 1846
- Stark D. P. et al., 2015b, *MNRAS*, 454, 1393
- Stark D. P. et al., 2017, *MNRAS*, 464, 469
- Terlevich E., Fernández-Arenas D., Terlevich R., Gieles M., Chávez R., González-Morán A. L., 2018, *MNRAS*, 481, 268
- Tosi M., Sabbi E., Bellazzini M., Aloisi A., Greggio L., Leitherer C., Montegriffo P., 2001, *AJ*, 122, 1271
- Trenti M., Padoan P., Jimenez R., 2015, *ApJ*, 808, L35
- Vanzella E., De Barros S., Cupani G. et al., 2016a, *ApJ*, 821, L27
- Vanzella E. et al., 2016b, *ApJ*, 825, 41
- Vanzella E. et al., 2017a, *MNRAS*, 465, 3803
- Vanzella E. et al., 2017b, *MNRAS*, 467, 4304
- Vanzella E. et al., 2017c, *ApJ*, 842, 47
- Vanzella E. et al., 2018, *MNRAS*, 476, L15
- Verhamme A., Schaerer D., Maselli A., 2006, *A&A*, 460, 397
- Yue B., Ferrara A., Vanzella E., Salvaterra R., 2014, *MNRAS*, 443, L20
- Zaritsky D., Crnojević D., Sand D. J., 2016, *ApJ*, 826, L9
- Zick T. O., Weisz D. R., Boylan-Kolchin M., 2018, *MNRAS*, 477, 480

APPENDIX A: ADDITIONAL MORPHOLOGICAL ANALYSIS OF D1

In this section, we run GALFIT on mock images inserted nearby D1. One thousand fake images have been inserted near D1, each of them resembling the D1(core) in both terms of magnitude and light profile index ($n = 0.5$), but adopting different R_c . The simu-

lated images have been inserted avoiding evident sources already present in the *F105W* image (extracted from the Astrodeep catalogue; Castellano et al. 2016). We then performed the simulation in two ways: (1) the procedure described in Section 2.2.3 has been performed for each image by running GALFIT on a grid of parameters and deriving the customized standard deviation and (2) by running GALFIT leaving its internal minimization procedure and starting from free parameters. The aim is to replicate on mock images the same procedures we used for D1(core) (Section 2.2.3).

In case (1) the behaviour of the standard deviation is shown as a function of the R_e for five sets of 1000 images, $R_e = 3, 2, 1, 0.75, 0.5$ pixel and using two PSFs. The best solutions (minimum error) occur at $R_e \lesssim 1$ pixel. The sub-pixel cases are marginally recovered and the minimum error disappears as half a pixel is approached (see Fig. A1). When compared to the results we obtained on D1(core) above, this exercise suggests that R_e is smaller than 1 pixel (otherwise it would have been recognized). These tests have been performed using the same PSF in the construction of the mock images and in the recovering process and as expected no systematic errors are present (Fig. A1 shows the best solutions that fall exactly on the input radii). We then performed the same simulation by using our PSF (FWHM = 0.18 arcsec) and the Anderson model (FWHM = 0.16 arcsec). The effect is shown in Fig. A1 (left-hand panel) with red arrows indicating the shifted position of the minimum standard deviation. Clearly, if a broader/narrower PSF is adopted in recovering the morphology, the resulting R_e would be underestimated/overestimated. The PSF constructed using the stars present in the field (and hence including the same reduction process as for the target) is the closest to the effective PSF in our image (FWHM = 0.18 arcsec, that is also consistent with what cal-

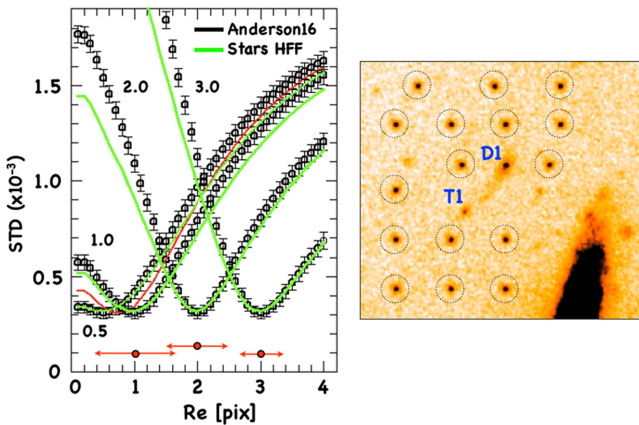


Figure A1. The right-hand panel shows an example of mock images used in the MC simulation (dotted circles). On the left-hand side, we show the standard deviation as a function of R_e (in the interval 0.1–4 pixel with $\Delta R_e = 0.1$ pixel), from MC simulations of 1000 fake images with different input $R_e = 3, 2, 1,$ and 0.5 pixel, as done for D1(core) (Fig. 5). The black circles with errorbars are the averaged standard deviation and dispersion of 1000 GALFIT runs, at fixed n and magnitude. The input R_e values are reported near the curves (in pixel) and are well recovered with the minimum standard deviation in correspondence of the input R_e . Sub-pixel radii are marginally (or not) recovered when half a pixel is approached. Black and green colours represent the same MC performed with two PSFs, the model PSF from Anderson and our HFF-based one. The horizontal red arrows (with arbitrary position in the Y-axis) show the systematic effect (direction and module) in recovering the input R_e when a different PSF (wider or narrower) are used in the reconstruction.

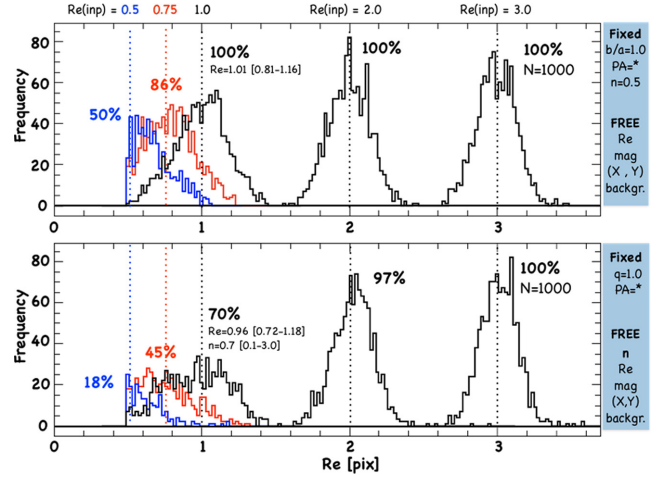


Figure A2. GALFIT fitting on the 1000 mock images allowing for its internal minimization procedure. When a GALFIT warning was obtained (corresponding to $R_e < 0.5$ pixel), the fit was not considered. The top panel shows the recovered R_e for five sets of 1000 images, with $R_e = 3, 2, 1, 0.75,$ and 0.5 pixel, fixing $PA, q,$ and $n = 0.5$ (to the input values). In the bottom panel PA and q are kept fixed (see the legend in the right-hand side). Images with $R_e = 1$ pixel are fully recovered, although with a wider spread. At sub-pixel scales the number of failures increases (warnings on R_e and/or n), however, the median still approaches the true value. This test is fully consistent with the results shown in Fig. 5, suggesting the R_e of D1(core) is less than 1 pixel (13 pc).

culated by Merlin et al. 2016 using the same HFF data). A similar result is achieved in the case (2), where GALFIT recovers the input radius down to $R_e = 1$ pixel. GALFIT has been run by fixing PA and q (bottom panel of Fig. A2) or by fixing $PA, q,$ and $n = 0.5$ (top panel of Fig. A2). In particular, a solution is reached for 100 per cent of the 1000 images in the case of $R_e = 3, 2,$ and 1 pixel (with fixed $PA, q,$ and $n = 0.5$). The sub-pixel images ($R_e = 0.5, 0.75$ pixel) are partially recovered, though with an increasing failure as R_e approaches half a pixel (a failure in the fit is provided by an internal warning flag produced by GALFIT; Peng et al. 2010).

APPENDIX B: SED-FITTING OF D1(CORE)

As discussed in Section 2.3.2, the SED-fitting has been performed for the object D1 and the SFR of D1(core) was inferred by rescaling properly the results from D1. Here, we show the resulting physical properties from the SED-fitting applied directly to the extracted photometry of the core, excluding the Ks and the *Spitzer*/IRAC bands, not informative in this process. The degeneracy among the stellar mass, age, and star formation rate is evident (Fig. B1), in which both D1 and D1(core) follow a similar behaviour. The current spatial resolution in the MUSE data cube prevents us from measuring the $Ly\alpha$ flux separating among D1 and D1(core). Therefore, as discussed in the main text (Section 2.3.1) a limit on the age and SFR can be obtained only for D1. The best-fitting solution for D1(core) suggests a stellar mass of $\simeq 0.8 \times 10^6 M_\odot$, an age younger than 10 Myr and an SFR of $0.35 M_\odot \text{ yr}^{-1}$, the latter spanning the 3σ range of $0.06\text{--}3.5 M_\odot \text{ yr}^{-1}$ (the stellar mass and the SFR shown in Fig. B1 are observed quantities, the intrinsic ones are obtainable by dividing the observed ones by $\mu_{\text{tot}} = 17.4$). Adopting the best estimate of the SFR and the upper limit on the

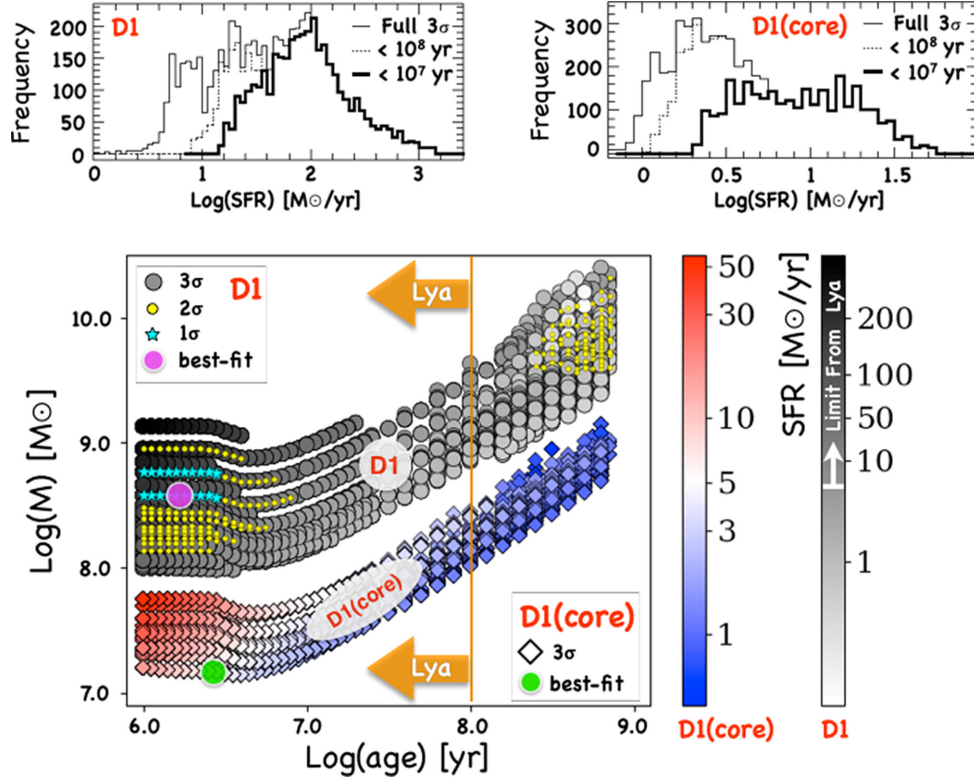


Figure B1. The same as Fig. 7 in which the results within 3σ of the SED-fitting on D1 (grey-coded) and D1(core) (colour-coded) are shown. In the top panels, the 3σ distributions of the SFRs are shown, including those with selected upper ages of 10 and 100 Myr. The magenta and green circles mark the best-fitting solutions for D1 and D1(core), respectively.

effective radius of the core (Section 2.2.3), $\text{Log}_{10}(\Sigma_{\text{SFR}})$ turns out to be higher than 2.4, fully consistent with the distribution shown in Fig. 9, lying in the upper part of the diagram populated by the

densest known star-forming objects, including young massive star clusters and ultracompact dwarf galaxies.

This paper has been typeset from a $\text{T}_{\text{E}}\text{X}/\text{L}_{\text{A}}\text{T}_{\text{E}}\text{X}$ file prepared by the author.